
Hadronic Dark Matter Searches at CMS at $\sqrt{s} = 13 \text{ TeV}$

Searches for invisibly decaying Higgs bosons and semi-visible jets

By

ESHWEN BHAL



School of Physics
UNIVERSITY OF BRISTOL

A dissertation submitted to the University of Bristol in
accordance with the requirements for award of the degree
of DOCTOR OF PHILOSOPHY in the Faculty of Science.

APRIL 2020

Word count: number in words

ABSTRACT

H ere goes the abstract

DEDICATION AND ACKNOWLEDGEMENTS

This work is dedicated to my grandfather, Dato' Mahindar Singh Bhal, who was able to begin this journey with me but sadly unable to finish it. There are far too many people and too little space to individually thank everyone who has accompanied me during this PhD, but I'll try my best.

Firstly, to my supervisor, Dr. Henning Flächer. Your advice and guidance over the course of this degree has been instrumental to achieving it, as well as encouraging my growth as a researcher.

Secondly, to all my colleagues at the University of Bristol. Very little would have been achieved without your help. From scientific discussions in the pub to pub discussions in the physics building, they have all been fruitful either directly or by helping me detach from work. Special thanks are in order to Simone and Sam Maddrell-Mander in my cohort, who have put up with my complaining during the stressful times.

To my friends from Monmouth that include my best friends in the world, Mike, James, Sneddon, (Mini) Sam, and Matt Bristow. You've been on this adventure with me since our school days and had my back the entire time. We've been through the highest, lowest, and most hilarious times together. I can definitively say I would not be the person I am today without you.

To my friends from LTA and those based at CERN, especially Dwayne, Vukasin, and Matt Heath. You became my second family while I was in Geneva. I'll miss the skiing, trips into the city, games, and general banter.

To my undergraduate cohort from Exeter. Though our meet ups are rare, I always look forward to our group holidays and hope they continue far into the future.

Lorenza Iacobuzio, you get a special mention. While we weren't especially close until recently, you've been my sage, partner in food, and exceptional friend when I've needed it the most.

Finally, and most importantly, my family deserve my thanks. You have been there for me since the very beginning supporting me through school, undergrad, PhD, and every other endeavour. To my grandparents, uncles, aunties, and cousins, my siblings Joe, Lydia, Sitara, and Arjen, my stepmum Nadia, and my cat Pixie, I am sincerely grateful to have you in my lives. But above all else, to my mum Meeta and dad Kiron, I could not have done any of this without you and as such, you have my deepest and most heartfelt love and gratitude.

AUTHOR'S DECLARATION

I declare that the work in this dissertation was carried out in accordance with the requirements of the University's *Regulations and Code of Practice for Research Degree Programmes* and that it has not been submitted for any other academic award. Except where indicated by specific reference in the text, the work is the candidate's own work. Work done in collaboration with, or with the assistance of, others, is indicated as such. Any views expressed in the dissertation are those of the author.

SIGNED: DATE:

TABLE OF CONTENTS

	Page
List of Figures	ix
List of Tables	xi
1 Introduction	1
1.1 Evidence for dark matter	1
1.1.1 Alternative theories to dark matter	3
1.2 Overview of dark matter searches	3
1.2.1 Dark matter searches at the LHC	5
2 Theory	7
2.1 The standard model of particle physics	7
2.1.1 Limitations of the standard model	7
2.2 Theoretical motivations for, and descriptions of, dark matter	8
2.3 Important observables in collider physics	9
2.3.1 Transverse momentum (p_T)	9
2.3.2 H_T	10
2.3.3 Missing transverse momentum (p_T^{miss})	10
2.4 Measuring the branching ratio of invisibly decaying Higgs bosons	10
2.5 Searches for semi-visible jets	12
2.5.1 Kinematics and free parameters of the model	13
3 The LHC and the CMS experiment	17
3.1 CERN	17
3.2 The Large Hadron Collider	19
3.2.1 A proton's journey	19
3.2.2 Luminosity	20

TABLE OF CONTENTS

3.2.3	Pileup	22
3.2.4	Evolution of the LHC	23
3.3	The CMS experiment	25
3.3.1	The CMS detector	25
3.3.2	Data acquisition and triggering	29
3.3.3	Simulating CMS data	32
3.3.4	Jet energy corrections in the Level-1 Trigger	33
4	Combined search for invisibly decaying Higgs bosons in hadronic channels	37
4.1	Analysis overview	38
4.1.1	Hadronic production modes of the Higgs boson	38
4.2	Categorisation of the non-VBF production modes	38
4.3	Data and simulation	38
4.3.1	Weights and corrections for simulated processes	38
4.4	Triggers	42
4.5	Background estimation	42
4.5.1	Control regions	42
4.5.2	Sidebands to the signal region	42
4.5.3	Background estimation methods	42
5	Search for dark matter through the production of semi-visible jets	43
5.1	Analysis overview	44
5.2	Data and simulation	44
5.2.1	Generating signal samples in PYTHIA	44
5.2.2	Generating signal samples in MADGRAPH	44
5.2.3	Triggers	44
5.3	Background estimation	44
6	Conclusions	45
A	Appendix A	47
	Bibliography	49
	Glossary	59
	Acronyms	61

LIST OF FIGURES

FIGURE	Page
1.1 A visual representation of the three main types of dark matter detection: direct, indirect, and production	4
1.2 The expected masses and interaction cross sections of some dark matter candidates. The centre of mass energy of the LHC is best suited to targeting WIMPs	6
2.1 A measure of WIMP dark matter comoving number density as a function of time with projections for different particle masses	9
2.2 Example Feynman diagrams for the two main production modes of semi-visible jets. A Z' boson mediates the s -channel process while a bi-fundamental Φ mediates the t -channel process	13
2.3 The constituents of a semi-visible jet as a function of its invisible fraction	14
2.4 The typical direction of the missing transverse energy relative to the semi-visible jets as a function of the invisible fraction r_{inv}	14
3.1 A schematic of the CERN accelerator complex	21
3.2 The average number of pileup interactions at CMS during 2015 and Run-2 of the LHC	23
3.3 The integrated luminosity of pp collision data delivered to CMS during Run-2 of the LHC	24
3.4 A cutaway diagram of the CMS detector with all of the principal components labelled. This detector configuration was used for the 2017–18 data taking years	26
3.5 A transverse slice through the CMS detector with the main subsystems and components visible	28
3.6 A quadrant of the CMS detector showing the main subsystems with their radius R , longitudinal distance z , and pseudorapidity η from the interaction point	29
3.7 A summary of the CMS Level-1 Trigger data flow from the hits recorded by the subsystems to the Global Trigger	31

LIST OF FIGURES

3.8 Examples of correction curves used to calibrate the jet energies in two $ \eta $ bins	35
3.9 The energies of matched pairs of jets in the entire barrel and end cap, in the pileup 40–50 range, before and after jet energy corrections have been applied	35
3.10 The response curves in each $ \eta $ bin as a function of p_T^{L1} , in the pileup 40–50 range, before and after jet energy corrections are applied	36
4.1 The Feynman diagrams for the four main hadronic production modes of the Higgs boson	39

LIST OF TABLES

TABLE	Page
3.1 The integrated luminosity delivered by the LHC during Run-2 which were recorded and certified by CMS	24
3.2 Some of the important parameters defining the performance of the LHC at the end of Run-2, for the High-Luminosity LHC and the design specification	25

INTRODUCTION

The universe, in all its vastness, structure, natural laws and chaos, is comprised of only three principal components: visible matter, the ingredients of stars, planets and life, is the only one we interact with on a regular basis; dark energy, a force or manifestation of something even more mysterious, responsible for the accelerating expansion of the universe, is almost entirely unknown; and dark matter, a substance invisible in all sense of the word, that binds galaxies together and influences large scale structure in the cosmos, is the focus of this thesis.

1.1 Evidence for dark matter

The earliest evidence for a large, non-luminous component of the galaxy stretches back to the 1920s when Jacobus Kapteyn attempted to explain the motion of stars in the Milky Way [77]. Since then, a wealth of independent astrophysical observations have reinforced the existence of this aggregation not just in our own, but in countless other galaxies and cosmological bodies. The Coma Cluster is a famous example: 90 % of its mass is thought to arise from dark matter, confirmed by its large mass-to-light ratio of $400 M_{\odot}/L_{\odot}$ [106]. Further evidence is that the rotation curves of most galaxies are roughly flat [90], contrary to the expected Keplerian curve ($v_r \propto r^{-1/2}$) expected from solely visible matter. On a galactic scale, dark matter is sprinkled in a mostly spherical halo that spans beyond the observable disc. The inclusive dark matter mass increases linearly [56] to compensate for the decline expressed by visible matter [32, 61]. Gravitational lensing is another observational tool subject to

influence from dark matter. Images of galaxies and other objects captured by this method appear distorted from a large gravitational field between the source and observer warping its local spacetime [74]. Arcs, ellipses and Einstein rings of smeared galaxies are often seen when dark matter is present.

While there are no widely-accepted estimations, it is believed that 85–95 % of the Milky Way is comprised of dark matter [23, 24, 75]. Though these approximations include non-visible identifiable matter such as dim stars, black holes and neutron stars, the term “dark matter” typically reserved for the non-luminous, *non-baryonic* segment that pervades the cosmos. From the latest results of the Planck mission, the energy density of the observable universe is composed of 26.5 % dark matter [8]. This result follows the Lambda cold dark matter (Λ CDM) model to describe the constituents and evolution of the universe, which is often referred to as the cosmological analog of the standard model of particle physics (SM). From the calculations, postulations, and observations presented above, the following properties of dark matter can be deduced:

- It is electrically neutral since it does not interact with electromagnetic radiation.
- It is cold (non-relativistic). Its velocity within galaxies is similar to the inhabiting stars [29, 72], since the combination of visible and dark matter drives the measured rotation curves. One small caveat is that galactic dark matter would be cold since a velocity above the gravitational escape velocity of the galaxy would eject high speed particles.
- It is stable, at least on the timescale of the current age of the universe. Dark matter production is postulated to have occurred only in the early universe via a thermal freeze out mechanism (see Chpt. 2.2). Hence, the remaining fraction has been present for a considerable time. Since most galaxies are dominated by dark matter and the gravitational influence from only the visible matter is too small to maintain itself, they could not have developed without it. This supports the idea of “bottom-up” structure formation in the universe; smaller galaxies form around gravitational potential wells provided by coalescing dark matter, then merge to form larger structures [105].
- Its interaction with matter and itself is very weak, or even non-existent. The Bullet Cluster — an astronomical object encompassed by two colliding galaxy clusters — is the best example of this inference. From measurements of predominantly x-ray emission and gravitational lensing, it was found that while there is substantial dark matter present, interaction with itself and the visible matter surrounding it was minimal at most [40]. A kinematic explanation for the spherical distribution and low velocity of dark matter

in galaxies can be explained by its collisionless nature. During the formation of a galaxy or stellar system, visible matter frequently collides, dissipating angular momentum and collapsing into a disc.

1.1.1 Alternative theories to dark matter

Though little is known about dark matter itself since all evidence stems from its gravitational influence, there are alternative theories that may explain the observations presented above. However, the scientific community can exclude many of these. Mismeasurements of the amount of baryonic matter such as neutrinos, neutrons, and interstellar gas are among the simpler propositions.

The neutrino flux from stars, as well as the cosmic neutrino background [104], are precise and well-tested [REF]. Even considering the upper limits on neutrino masses [86], they cannot make a significant contribution to the dark matter content in the universe. This is even discounting their highly relativistic nature, where myriad experimental evidence suggests dark matter is cold.

One can also use the Cosmic Microwave Background to calculate the average photon and neutrino densities, and Big Bang Nucleosynthesis calculations to determine the baryonic matter density (see Ref. 59 for results with the latest Planck mission data). These can be compared to other measurements, e.g., mass-to-light ratios averaged across the universe, to reveal a discrepancy [51].

Neutrons cannot contribute to dark matter because isolated neutrons are unstable, decaying in a matter of minutes [88]. Transforming into charged protons and electrons, they interact strongly with light and therefore contribute to the luminous matter content.

Modified Newtonian dynamics (MOND) is a hypothesis that aims to explain phenomena typically associated with dark matter instead by modifications to Newton's laws of motion. There exist many theories and interpretations derived from this principle, though any one strand that tries to explain an observation usually fails to satisfy other phenomena or apply to length scales that general relativity may predict well. For example, observations of the Bullet Cluster [40] have discredited many popular MOND models.

1.2 Overview of dark matter searches

While observational evidence has so far lain with astrophysics, a theoretical description and discovery of dark matter may fall into the realm of particle physics with the numerous, novel

experimental searches underway. The detection of dark matter can be classified into three distinct methods with unique signatures (with a visual summary in Fig. 1.1):

- **Direct:** dark matter may interact with visible matter on small scales, scattering SM particles [92]. The recoil these SM particles experience could be detected by highly-sensitive, low background experiments such as LUX-ZEPLIN (LZ) [10] that specialises in the search for WIMP dark matter at a large range of masses.
- **Indirect:** if dark matter interacts with itself, it may annihilate to produce showers of high energy photons or pions. Background estimation is difficult since the signatures can be highly model-dependent. The photons may be of a continuum — from hadronisation and radiation of the decay products — or contain features, such as internal radiation from the propagator in the interaction or from loop-level processes [50]. Large ranges of the annihilation cross section and dark matter mass can be probed with telescopes already searching for these characteristic events.
- **Production:** dark matter may have been abundantly produced in the hot, early universe. High energy particle accelerators such as the LHC can reproduce these conditions, with the WIMP miracle (see Chpt. 2.2) reinforcing the idea that dark matter may exist in these accessible mass ranges. Many beyond the standard model (BSM) theories accommodate dark matter candidates with a diverse spectrum of final states that can be investigated by analysing LHC data.

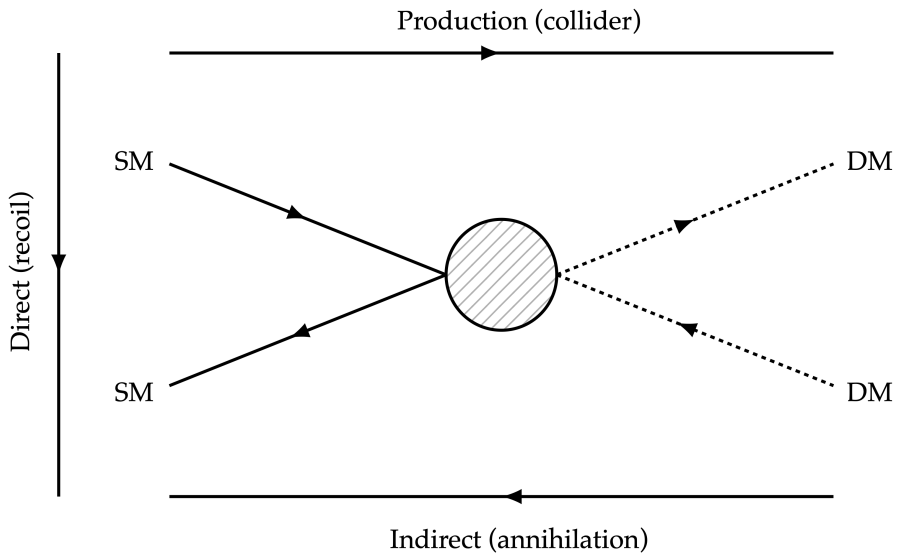


Figure 1.1: A visual representation of the three main types of dark matter detection: direct (dark matter recoiling from standard model particles); indirect (annihilation of dark matter); and production (dark matter created in high energy physics collisions).

1.2.1 Dark matter searches at the LHC

Since its detection at the CMS experiment from the production mechanism is the focus of this thesis, it is important to establish the current state of dark matter searches at the Large Hadron Collider (LHC), the world’s most powerful particle accelerator that provides data for CMS. Both machines are described in detail in Chpt. 3, and as such only a summary will be provided here. The LHC principally collides protons at centre of mass energies up to $\sqrt{s} = 13$ TeV. These exceptionally high energies allow the conditions in the very early universe to be simulated in which heavy, unstable particles were created in abundance. As such, many theories can be investigated that postulate heavy particles that do not exist in the universe today. Some of these, such as supersymmetry (SUSY) [85], sterile neutrinos [55], and Kaluza-Klein states [67] contain dark matter candidates that can be specifically searched for, or indirectly discovered if a theory is experimentally proven. Despite the success of the standard model in explaining the natural world, it does not substantiate the existence of dark matter; hence why BSM theories are popular. Fig. 1.2 illustrates the masses and interaction cross sections of many dark matter candidates. Weakly Interacting Massive Particles (WIMPs) (highlighted by the purple rectangle) are the subject of many searches at the LHC since the expected mass ranges and cross sections are accessible there.

Two avenues are usually considered when attempting to discover dark matter: explicit searches for the signatures of dark matter production, and anomalies in precision measurements. The former is quite common, with many theories and models tested at the LHC’s general purpose detectors, ATLAS and CMS. Searches at CMS have been performed for promptly-decaying and “long-lived” supersymmetry in hadronic final states (in which I made contributions) [79, 95]. Searches for specific supersymmetric particles in a variety of decay modes have been conducted by both experiments [35]. In many of these cases, the lightest supersymmetric particle (LSP) is considered to be a dark matter candidate. R -parity conservation is predicted (or even enforced) in many SUSY models [85], which prevents the decay of LSP and any lighter, standard model particles that have been observed to be stable. While supersymmetry is the most popular BSM theory, due in part to its numerous interpretations and approaches for discovery, many others have also been explored at the LHC. From microscopic black holes [81], to [OTHERS], there are many strategies that have the potential to uproot the standard model. The analyses above are usually characterised by large “missing” transverse momentum (explained further in Chpt. 2.3.3), a quantity that represents the momenta of particles invisible to the detector, which include dark matter. In Chpt. 5, I discuss in detail a search for dark matter that utilises this variable.

Precision measurements of standard model parameters is the other method often consulted

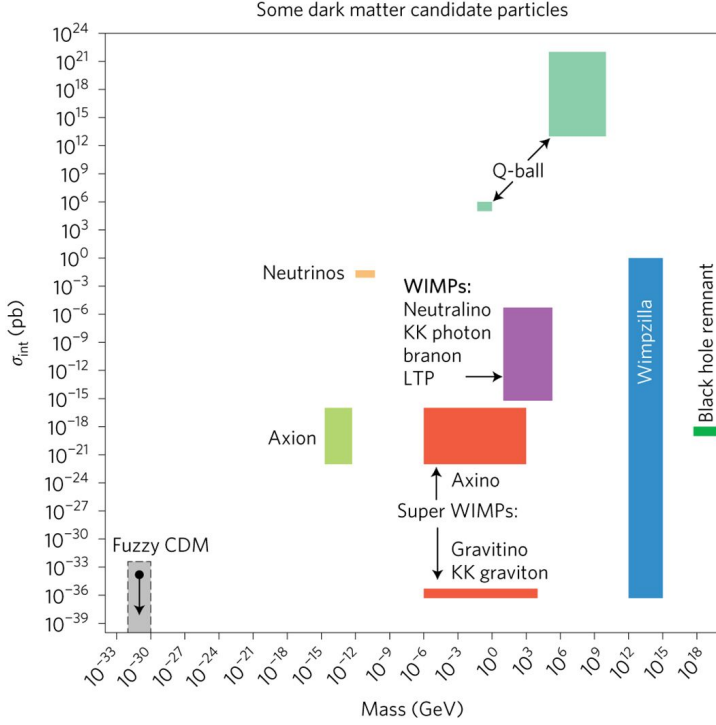


Figure 1.2: The expected masses and interaction cross sections of some dark matter candidates. The centre of mass energy of the LHC is best suited to targeting WIMPs. Figure acquired from Ref. 50.

in the hopes of attributing anomalies to new physics. For example, attempts to explain anomalies in the $b \rightarrow s$ transition include dark matter candidates [36, 103]. In Chpt. 4, I investigate how the measurement of the Higgs boson to invisible state branching ratio can accommodate dark matter.¹

There is significant motivation to study dark matter from a wider, as well as a more personal, viewpoint. It is important to understand how the universe operates, and dark matter opens up the potential for new physics that improves our understanding of nature. My personal interests include the blend of particle physics and astrophysics, and the opportunity to discover and add to humanity's collective wisdom. With 137 fb^{-1} from CMS during Run-2 at $\sqrt{s} = 13 \text{ TeV}$, there is great potential to constrain some of the properties of dark matter. This thesis showcases the motivation for, and results of, searches for invisibly decaying Higgs bosons and semi-visible jets with the full Run-2 dataset collected by the CMS experiment.²

¹Maybe add another example of anomalies in precision measurements

²Add another figure or two somewhere to help separate the text? Maybe an astronomical image of the Bullet Cluster/dark matter distribution in a cosmological object, or a gravitational lensing ring from dark matter

THEORY

This thesis is comprised of experimental searches for dark matter and new physics. The experimental chapters Chpt. 4 and Chpt. 5 delve deeply into the analyses. Before which, the theoretical and phenomenological motivations must be understood to [back up] the need for these searches at the Large Hadron Collider. In this chapter, a brief recap of the standard model will be [presented] along with its shortcomings, i.e., the lack of a dark matter candidate. Theoretical descriptions of dark matter that best fit the relic density and astrophysical observations will then be discussed. Specific interpretations in the form of semi-visible jets and invisibly decaying Higgs bosons are [looked at] that provide the background for the respective analysis chapters.

- Give an overview of the fundamental forces and particles.
- Discuss the Standard Model in some amount of detail, emphasizing certain aspects as they relate to dark matter and the Higgs field (and boson).

2.1 The standard model of particle physics

2.1.1 Limitations of the standard model

Despite the standard model providing precise predictions of three of the four fundamental forces and the particles that they interact with, there are many experimental observations that it cannot currently explain. Neutrino masses, dark matter, dark energy, and gravity all escape its description. Testing TeV TeV.

2.2 Theoretical motivations for, and descriptions of, dark matter

The universe may have birthed dark matter via one of many possible mechanisms. The most popular is described as a “thermal freeze-out” process. In the hot, early universe when the thermal background allowed spontaneous pair production of particle dark matter, it was produced in abundance. During this period, the particles may also have frequently annihilated since the cosmos was still small. Inevitably, the universe expanded and cooled; the temperature became too low to allow significant production [21]. Matter was further separated and the dark matter annihilation rate decreased, leaving behind the “thermal relic” that is observed today. These remaining particles were attracted via gravity, forming filaments throughout the universe. The potential wells they induced allowed the progenitors of galaxies to form within.

Full derivations of the thermal freeze-out of dark matter¹ can be found in literature [26, 63], with the “WIMP miracle” as a consequence: with relatively few assumptions, the correct dark matter relic abundance can be recovered by requiring a WIMP mass of $\mathcal{O}(\text{GeV} - \text{TeV})$, dependent on the annihilation cross section. This is a range accessible at contemporary colliders such as the LHC, and perhaps coincidentally, around the electroweak energy scale. It is common for figures that depict the WIMP dark matter density over time to plot the “yield” n_χ/s as a function of the dimensionless parameter $x = m_\chi/T$. In the former variable, n_χ is the number density and s is the entropy density. In the latter, m_χ is the dark matter mass and T is the average temperature of the universe, which serves as a measure of its age since the temperature decreases over time. An example is given in Fig. 2.1.

The time of the dark matter freeze out epoch is somewhat insensitive to the mass and annihilation cross section. Approximate solutions to the Boltzmann equation for time-dependent n_χ — where dark matter is modelled as a weakly-interacting, diffuse gas of particles — suggest $x_f \sim 20$ [26, 84]. Stronger dark matter interaction leads to decoupling at a later time and a lower number density. The approximate value of x_f is significant in that it supports the electroweak-scale mass of WIMPs.

Another popular mechanism, targeting low-mass dark matter, is the “freeze-in” process [65, 82]. In this [scenario], dark matter is not produced thermally in the early universe. Instead, it emerges through interactions between SM particles such as collisions, or decays of those heavier than dark matter. The comoving density increases with time until it plateaus because

¹Is it worth going through the derivation, maybe as an appendix? It might be superfluous considering it’s already described in literature.

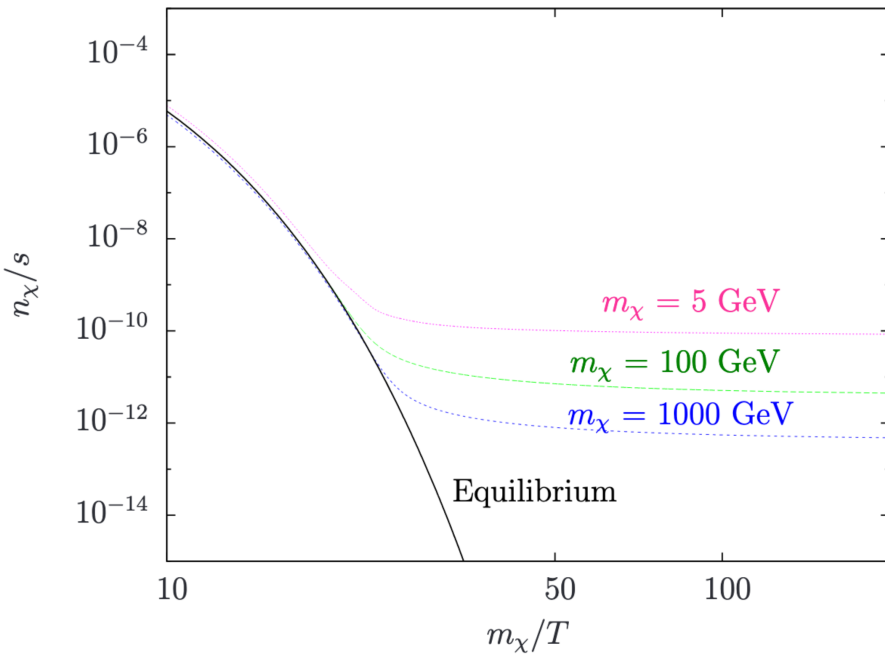


Figure 2.1: A measure of WIMP dark matter comoving number density as a function of time with projections for different particle masses. A higher mass must be balanced by a larger annihilation cross section to achieve the correct relic density, to which it tends asymptotically from the point of thermal freeze out. The black curve represents the scenario in which dark matter remains in equilibrium with the standard model. Figure taken from Ref. 66.

of the cooling of the universe, where SM particles are generally stable enough and too low energy to produce dark matter in any meaningful quantity. The relic abundance can therefore be reclaimed from a combination of the initial thermal distributions, the dark matter mass, and the interaction strength, similar to the freeze-out process. In order to obey cosmological observations, particularly the fact that it is cold, the masses freeze-out dark matter particles are expected to be $\mathcal{O}(\text{keV})$ or heavier.

2.3 Important observables in collider physics

2.3.1 Transverse momentum (p_T)

In the LHC (or any other collider), the longitudinal momentum of the initial state particles is typically unknown. However, the momentum transverse to the beam is zero before the collision, and therefore must be zero afterward due to momentum conservation. This is why the transverse momentum of a particle or physics object (\vec{p}_T for the vector quantity, p_T for its magnitude) is a useful variable in an analysis.

2.3.2 H_T

The scalar sum of the transverse momentum of hadronic constituents in an event, i.e., the jets, is symbolised as H_T . It is often used in analyses focused on hadronic objects, such as natural supersymmetry in which a large jet multiplicity is expected. Formally,

$$(2.1) \quad H_T \equiv \sum_{\text{jets}} p_T$$

Typically, a lower limit on p_T is used when calculating the H_T , so jets below this threshold do not factor into the sum. This is to avoid low momentum jets attributed to pileup events (see Chpt. 3.2.3), and those from the primary vertex that can often be mismeasured.

2.3.3 Missing transverse momentum (p_T^{miss})

The missing transverse momentum p_T^{miss} is defined as the negative vector sum of the p_T of all identified particles in an event. It is a term often used interchangeably with missing transverse energy (MET, E_T^{miss}). Undetected particles from neutrinos or dark matter, or mismeasured kinematic properties of identified particles, will introduce an imbalance in the vector sum of the p_T . Hence, the p_T^{miss} will be non-zero. Formally,

$$(2.2) \quad p_T^{\text{miss}} \equiv - \sum_i^{N_{\text{particles}}} \vec{p}_{T,i}$$

The hadronic-only counterpart to this variable, H_T^{miss} , is the negative vector sum of the jet transverse momenta in an event:

$$(2.3) \quad H_T^{\text{miss}} \equiv - \sum_j^{N_{\text{jets}}} \vec{p}_{T,j}$$

As with H_T , the H_T^{miss} is often calculated with a lower limit on the jet p_T .

2.4 Measuring the branching ratio of invisibly decaying Higgs bosons

The Higgs boson has caught the attention of the high energy physics community and even the public eye like no other particle in recent memory. Its discovery in the $H \rightarrow \gamma\gamma$ channel

2.4. MEASURING THE BRANCHING RATIO OF INVISIBLY DECAYING HIGGS BOSONS

in 2012 by both CMS [38] and ATLAS [5] independently realised one of the [principal] goals of the LHC’s construction. The particle itself is not necessarily exciting. Rather, it confirms the existence of the Higgs *field* that pervades the universe and gives mass to the elementary particles via the exchange of its namesake boson [57, 64, 73]. [Its discovery], one might think, was the end of the discussion of the Higgs boson. However, it was only the beginning.

Many observations of the Higgs, such as its predominant decay mode $H \rightarrow b\bar{b}$, were not seen until recently (CMS [93], ATLAS [4]). Constraints on its other properties have also been placed, such as its resonance width and branching ratios \mathcal{B} to other final states. Fully understanding the Higgs boson is important to understanding the Higgs field and the wider standard model. Precision measurements in tension with SM predictions can also be a window to new physics. Measuring the $H \rightarrow \text{inv.}$ branching ratio aims to do just that.

The only SM process in which Higgs boson can decay invisibly² is $H \rightarrow ZZ \rightarrow 4\nu$ with a branching ratio of $\mathcal{O}(0.1\%)$ [70]. The leading observed experimental upper limits on this measurement are 19 % from CMS [97] and 26 % from ATLAS [3], far above the predicted value. If undiscovered invisible particles, perhaps dark matter, couple to the Higgs field the branching ratio will be enhanced.³ Experimental evidence shows the coupling strength to proportionally follow the mass of the particle, as verified in ATLAS and CMS’ latest measurements [100]. A considerably large enhancement may allow for this process to be observed at the LHC. At the very least, a more accurate constraint on the branching ratio is able to exclude some models of dark matter, such as those described in Refs. 54, 76.

There is no reason to assume dark matter does *not* interact with the Higgs field, since it bestows mass to all known elementary particles (a small caveat, perhaps, being neutrinos).⁴ Higgs “portal” models have been theorised that connect the visible sector of the standard model to a dark sector where particle dark matter resides [16, 19]. Certain models also predict a detectable presence at the LHC from a sufficient production rate [31], perhaps even with data obtained during Run-2 [7].

²A direct decay to neutrinos is possible if they acquire their mass from the Higgs field. But as the upper limit on the SM neutrino masses is very small, the branching ratio is expected to follow suit.

³Do I need to give a more mathematical motivation for the BR being enhanced/what kind of values the BR is expected to be from various DM models?

⁴Do I need to give some mathematical motivation as to *why* dark matter would couple to the Higgs? Or is the fact that it has mass enough justification?

2.5 Searches for semi-visible jets

Many searches for dark matter presume it is a WIMP-like particle because of the considerations discussed in Chpt. 2.2. In the LHC, the signatures of WIMPs would be driven by large missing transverse momentum recoiling from visible matter in the event. Monojet [80] and dijet [96] searches are able to exploit this, for example. However, no sign of WIMPs have been observed yet. Thankfully, a boundless supply of [other] theories exist, with possible signatures equally as varied. Though the p_T^{miss} could still be one of the characteristics by which the dark matter can be inferred, a plethora of topologies and discriminating observables are possible. The dynamics that govern dark matter may be confined to a “dark sector” or “hidden sector”, inhabited by new forces and particles.

A dark sector may be largely inaccessible (as in some Hidden Valley⁵ scenarios [101]), but communicate with the visible sector through a portal interaction. An example from SM particles could be the Higgs boson bridging the visible and hidden sectors, as mentioned in Chpt. 2.4. Many interesting and novel signatures can be probed in LHC experiments from models like these. Dark forces with energy scales in the tens of GeV (gigaelectron volts) and mediator masses up to TeV (teraelectron volts) may be accessible. If they are analogous with the standard model, the mechanisms can be explained for the dark matter presence and relic density arising from a baryon-like asymmetry.

Proposed in Refs. 41, 42, a strongly-coupled dark sector in a Hidden Valley scenario is imagined with interactions analogous to QCD.⁶ The portals allowing the dark and visible sectors to communicate can be decomposed into a leptophobic Z' (s -channel) and bi-fundamental Φ (t -channel) mediator. In the t -channel case, Φ is a representation of both the visible and dark QCD gauge groups. Depictions of the processes above are given in Fig. 2.2. In the LHC, protons could collide at energies high enough to access the dark sector. From either the resonant production of a Z' or exchange of a Φ , dark quarks χ are produced. Below a dark confinement scale Λ_{dark} , hadronisation takes place into dark hadrons. Depending on the species, some of these dark hadrons are stable (i.e., a source of dark matter), while others are unstable and decay back into visible sector particles, namely standard model quarks. The final state is then a shower of two jets each interspersed with dark matter: *semi-visible jets*.

⁵A Hidden Valley is a schema where the standard model is extended by a non-abelian group. SM particles are uncharged under this group. The new, light particles from this extension are the opposite: charged under the new group and neutral under the SM gauge group. A heavy mediator carries both charges, acting as a portal between the standard model and Hidden Valley particles.

⁶Do I need to mention that this dark sector is $SU(2)_{\text{dark}}$, and write the lagrangian for how it couples to SM via dark weak force?

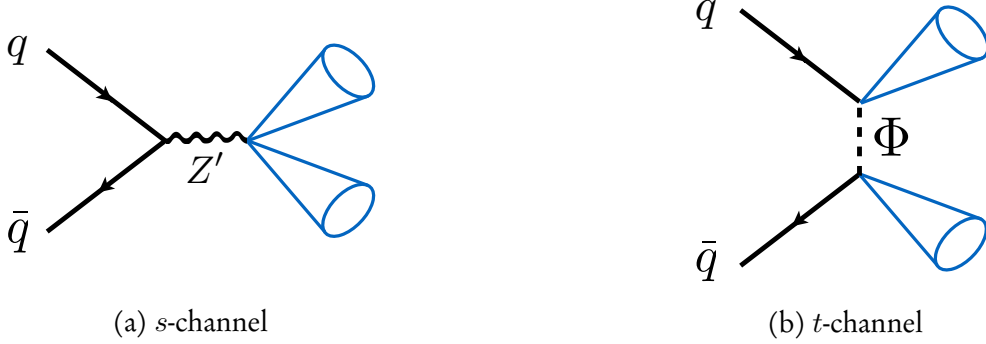


Figure 2.2: Example Feynman diagrams for the two main production modes of semi-visible jets [42]. A Z' boson mediates the *s*-channel process while a bi-fundamental Φ mediates the *t*-channel process.

2.5.1 Kinematics and free parameters of the model

The kinematics of semi-visible jets are heavily influenced by the [main] free parameters of the model: the mass of the mediator ($m_{Z'}$ or m_Φ), the dark coupling strength (α_{dark}), the dark quark mass (m_χ), and the invisible fraction (r_{inv}).

- $m_{Z'}/m_\Phi$: Since the energies of the colliding protons have an upper limit, the conservation of energy (or momentum) imposes one on the on-shell production/exchange of the mediator particle. In the *s*-channel process, the Z' production is resonant. Consequently, its mass is possible to recover by calculating the dijet mass m_{jj} or transverse mass M_T .
- α_{dark} : In Ref. 42, this is defined as $g_{\text{dark}}^2/4\pi$ (where g_{dark} is the coupling constant between the dark quarks and mediator). As in QCD, the dark coupling runs as a function of the energy scale, influencing Λ_{dark} . At 1 TeV,

$$(2.4) \quad \Lambda_{\text{dark}} = 1000 \text{ [GeV]} \exp\left(\frac{-2\pi}{\alpha_{\text{dark}} b}\right)$$

where $b = \frac{11}{3}N_c - \frac{2}{3}N_f$ is related to the number of dark colours and flavours, respectively.

- m_χ : This parameter does not directly affect much, but is related to the dark hadron mass ($2m_\chi$) and Λ_{dark} . The combination of the two properties affects the shower dynamics. Note that while Ref. 42 describes some of these to be insensitive, a parameter scan over these two variables are necessary in the search described in Chpt. 5.
- r_{inv} : This is defined as the fraction of produced invisible particles that remain stable, at least over timescales where they interact with a detector. When generating simulated samples, r_{inv} can be interpreted as the *probability* of a dark hadron remaining stable.

While this variable is not inherent within the model, it is one that can encompass many underlying components. As a result, visualisation of the shower and direction of p_T^{miss} is much more intuitive, as demonstrated in Figs. 2.3 and 2.4, respectively. A large value of r_{inv} would yield a similar final state to a WIMP search.

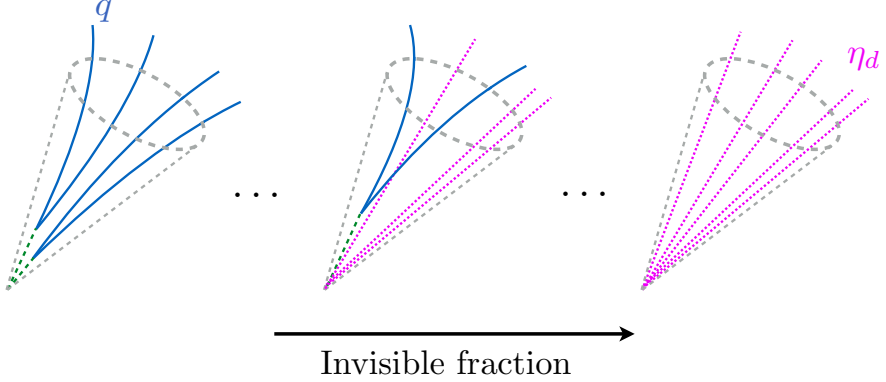


Figure 2.3: The constituents of a semi-visible jet as a function of its invisible fraction r_{inv} [42].

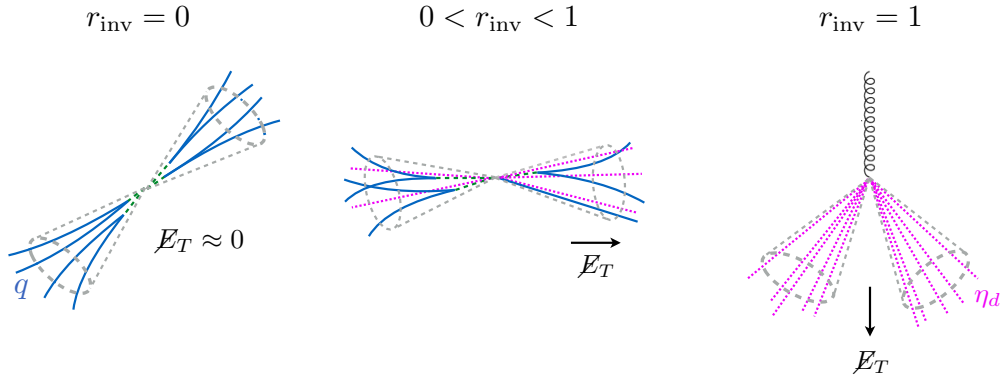


Figure 2.4: The typical direction of the missing transverse energy \cancel{E}_T (or p_T^{miss}) relative to the semi-visible jets as a function of their invisible fraction r_{inv} [42].

In the search for semi-visible jets in Chpt. 5, only the s -channel process has been analysed with LHC data. Generator studies have been additionally performed for the t -channel interaction and the analysis is underway. In the s -channel search, mediator masses of up to several TeV are accessible, and intermediate values of r_{inv} are most sensitive. Hence, the typical signature is a dijet pair with each jet likely to contain a different invisible fraction, leading to the p_T^{miss} aligned with one of the jets. WIMPs, on the other hand, completely recoil from the visible matter, and so jets may be more collimated with small separation. The p_T^{miss} is also

larger and possibly more isolated. The phase space exploited by this model is often rejected by dark matter searches since the final state can be easily mimicked by mismeasured QCD. A sizeable background from this process would therefore be present. However, jet substructure techniques and machine learning algorithms have developed rapidly in the recent years, and it is possible to disentangle signal and background with some certainty.

One interesting aspect of the model is the potential for signatures with displaced vertices, so called “long-lived” particles or “emerging jets” since the decay into visible states occurs a sufficient distance from the primary vertex. Some searches have already been performed for this final state from a different interpretation of strongly-coupled dark forces [98] to supersymmetry contexts [95]. These are not considered in Chpt. 5, so the dark hadrons are assumed to decay promptly. Long-lived interpretations have been noted as possible extensions to the search, however.

THE LHC AND THE CMS EXPERIMENT

This chapter concerns the experimental setup. CERN is the organisation that manages the machines discussed and is a pioneer in the high energy physics community. As such, it will be given a short overview. The Large Hadron Collider provides the CMS experiment with proton-proton collision data that is then stored, corrected, and then used by physicists for analyses. Ranging from standard model precision measurements, searches for new physics, the development of tools and algorithms to aid the previous two, these and much more are studied by the collaboration. CMS is described in detail, from its hardware and subdetectors to its data acquisition and trigger system. Special attention is given to the derivation of jet energy corrections (JEC) in the Level-1 Trigger (L1T) as I have been a part of that effort during my PhD.

- Emphasise the jet and energy sum triggers in Level-1 Trigger as I've worked on them, and Calorimeter Layer-2 for the same reason. Tie into SVJ and Hinv since they're hadronic searches.

3.1 CERN

CERN, the European Organisation for Nuclear Research (*Organisation Européenne pour la Recherche Nucléaire*), is the body responsible for large scale particle and high energy physics projects in Europe. It was founded in 1954 under the *Conseil Européen pour la Recherche Nucléaire* (European Council for Nuclear Research), from where its acronym derived. CERN's primary site is situated in the canton of Geneva and creeps over the Franco-

Swiss border. Its main purpose today is to provide physical and technological infrastructure for particle and high energy physics experiments. From large scale accelerators to extensive computing farms, CERN has grown into the largest laboratory for particle physics in the world. The organisation also provides a central community for the many researchers, engineers, and technicians to share ideas and collaborate effectively.

The organisation was founded by twelve European member states, the United Kingdom being one of them. It has since expanded to twenty three, encompassing most of western Europe and some of the continent’s east. Many more countries from across the globe are affiliated with CERN in some way, providing researchers, computing resources, and more. The member states and associated members contribute to CERN’s budget, to the tune of 1.2 billion Swiss Francs for the year 2020 [60].

Many important inventions and discoveries can be attributed to CERN and its personnel. Physics [achievements] include observations of weak neutral current interactions in 1973 [68, 69], paving the way for the W [17, 22] and Z [18, 20] boson discoveries with the UA1 and UA2 experiments in 1983. The number of light neutrino generations at the Large Electron-Positron Collider (LEP) in 1989 [102], and direct CP violation with the NA48 experiment in 1999 [58], were also observed. Tim Berners-Lee and Robert Cailliau are credited with inventing the World Wide Web — the ubiquitous service for accessing the internet — in 1989/90.

CERN is perhaps most widely known as the home of the Large Hadron Collider, the particle accelerator involved in the discovery of the Higgs boson [5, 38]. More is discussed in Chpt. 3.2. But CERN is still involved in many more undertakings. There are many fixed target experiments that use beams from the PS and SPS such as COMPASS (studies hadronic structure) and NA62, investigating rare decays of kaons. Experiments like ALPHA and AEGIS use antiprotons from the Antiproton Decelerator to study antimatter in detail. The ISOLDE facility at CERN delivers beams of radioactive ions to perform many nuclear physics experiments.

Concern is given not just to contemporary science, but also to the physics of tomorrow. The experiments and accelerators are frequently upgraded, for example LHC improvements documented in Chpt. 3.2.4. Future accelerators are also being discussed, such as the Future Circular Collider (FCC). The collider would use the LHC as a booster, with the final ring having a 90–100 km circumference and up to 100 TeV centre of mass energy. Proposals for the injectants are electron-positron beams (FCC-ee, $\sqrt{s} = 90\text{--}350 \text{ GeV}$), and proton-proton beams (FCC-hh, $\sqrt{s} = 100 \text{ TeV}$). Each option boasts its own merits, and in an integrated scenario the former may be used as an intermediate step toward the latter.

3.2 The Large Hadron Collider

Deep underground beneath the Franco-Swiss border lies the Large Hadron Collider (LHC), a synchrotron particle accelerator 27 km in circumference. As the largest machine in the world, the LHC stands as a testament to the importance of fundamental science and the dedication to which it is pursued. Predominantly a proton collider, lead and xenon ions have also been injected for novel and unique studies. Four primary experiments are situated at their own interaction points where the two beams of particles are brought into contact: CMS (Compact Muon Solenoid), a general purpose detector with interests in precision measurements, searches for new physics, and many other avenues; ATLAS (A Toroidal LHC ApparatuS), a counterpart to CMS at the antipode of the LHC ring; LHCb, designed to study the decay of B hadrons; and ALICE (A Large Ion Collider Experiment), primarily studying heavy ion collisions and the quark-gluon plasma.

Four additional, smaller experiments are stationed in the LHC ring that are much more specialised than the above mentioned: TOTEM (TOTal Elastic and diffractive cross section Measurement) shares the CMS cavern with three subdetectors positioned near the beam line, performing proton structure and interaction cross section studies; LHCf shares the ATLAS cavern and is concerned with detecting neutral pions in the forward direction to explain the origins of high energy cosmic rays; FASER (ForwArd Search ExpeRiment) is another forward-based detector near ATLAS and searches for light, weakly interacting particles; finally, MoEDAL (Monopole and Exotics Detector at the LHC) is installed in the LHCb cavern and aims to detect magnetic monopoles and other exotic particles.

The technical design report for the LHC can be found at Ref. [33], detailing the ring itself, infrastructure, general services, and the injector chain.

3.2.1 A proton's journey

A proton begins its journey as a hydrogen atom in a little, red bottle. Around 3×10^{14} protons are supplied to each beam in the LHC, with billions of refills available in this single container. Once the hydrogen atoms leave the source, they are stripped of their electrons, and [sent] to the linear accelerator LINAC2.¹ This is the start of a long voyage through the accelerator complex (visualised in Fig. 3.1).

Given a modest boost to 50 MeV (megaelectron volt), the protons are sequentially fed from LINAC2 into the Proton Synchrotron Booster (PSB) that accelerates them further to

¹As of the end of Run-2, LINAC2 has been decommissioned. It has been replaced by LINAC4 in preparation for Run-3.

1.4 GeV. Another upsurge is provided once the protons travel to the Proton Synchrotron (PS), this time to 26 GeV. Then the final energy increase received before entering the LHC comes from the Super Proton Synchrotron (SPS), leaving the protons at 450 GeV. Once injected into the LHC, they are finally accelerated to their peak energy of up to 6.5 TeV from a sequence of radio frequency cavities over the course of twenty minutes. The oscillation frequency of these cavities is precisely tuned and timed to give protons the appropriate kicks and accelerate them to the desired energy. Since there is a distribution of proton energies in the beam, those that enter a cavity slightly out of time with a different energy than expected consequently become sorted into “bunches”. The remainder of the LHC ring is used to steer the beam with the aid of over 1,200 liquid helium-cooled superconducting dipole magnets. It is also focused by almost 400 equivalently-cooled quadrupole magnets to increase the rate of proton collisions.

One beam consists of a “train” of up to 2,808 bunches spaced 25 ns apart, each with 115 billion protons. Using bunches provides an advantage to the experiments at each of the interaction points. Discrete collisions take place between bunches in the opposing beams at 40 MHz as opposed to an almost continuous stream of protons. This allows for estimates of pileup interactions that can be filtered out, and would otherwise introduce miscalculations of sums like p_T^{miss} and H_T . Each proton-proton collision is colloquially known as an “event”, with data recorded by each experiment separated into events.

3.2.2 Luminosity

The *luminosity* of a particle accelerator is, along with centre of mass energy, a quantitative measure of its performance. It is often used to denote the amount of data delivered, or the data collected by the receiving detector. A full derivation of this quantity can be found in Ref. 71, and as such, a summary is given here. The *instantaneous luminosity* \mathcal{L} , typically quoted in $\text{cm}^{-2}\text{s}^{-1}$, is defined as

$$(3.1) \quad \mathcal{L} = \frac{1}{\sigma_p} \frac{dN}{dt}$$

where N is the number of collisions and σ_p is the production cross section. In the LHC, because many final states are possible, σ_p is not generally known. It can be measured, however. A recent paper from LHCb measured the extrapolated inelastic cross section (which is the important component for LHC collisions) to be $75.4 \pm 5.4 \text{ mb}$ at $\sqrt{s} = 13 \text{ TeV}$ [6], allowing an estimate of the collision rate. For two colliding beams split into bunches with the constituents in each bunch distributed according to a gaussian profile,

3.2. THE LARGE HADRON COLLIDER

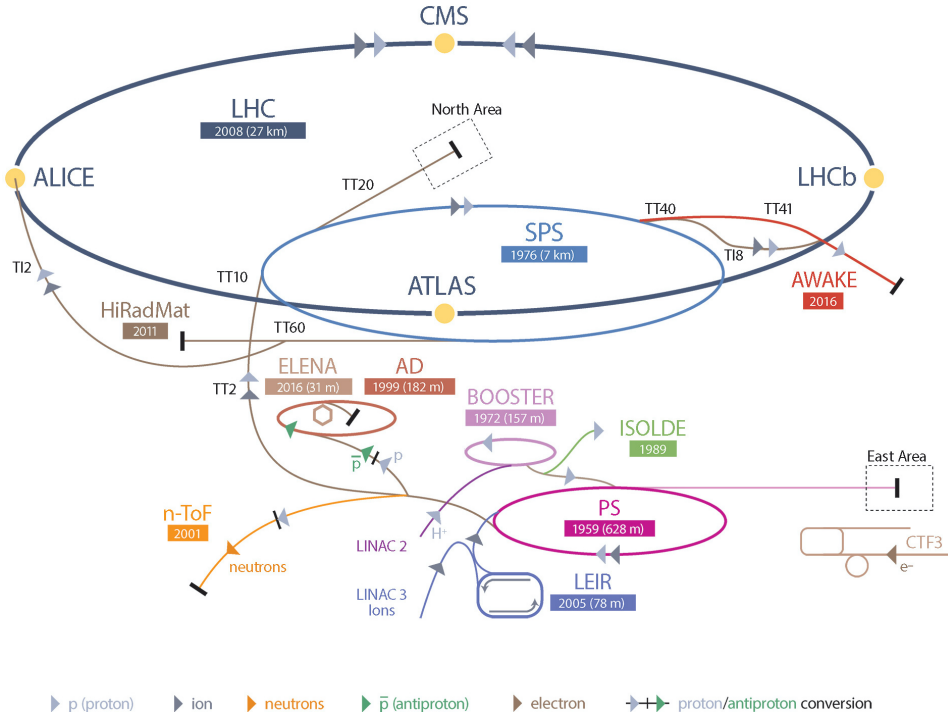


Figure 3.1: A schematic of the CERN accelerator complex. Various particles are shown from their sources to the detectors they are observed at. Figure obtained from Ref. 1.

$$(3.2) \quad \mathcal{L} = \frac{N_1 N_2 f N_b}{4\pi\sigma_x\sigma_y} \cdot F$$

where N_1 and N_2 are the number of particles in a bunch in beams 1 and 2, respectively, N_b is the number of bunches in a beam, f is the revolution frequency (11,245 Hz for protons in the LHC), and σ_x and σ_y are the horizontal and vertical sizes of the beam, respectively.²

The geometric reduction factor F is unity for beams colliding head on.³ However, in the LHC, the beams collide at an angle known as the “crossing angle” to reduce the effects of pileup. At the start of a fill when the number of protons in the LHC is at its maximum, the crossing angle at each interaction point is approximately 300 μ rad. As the runs progress, more protons collide and the luminosity decreases. One of measures taken to recover luminosity and keep the LHC as efficient as possible is to reduce the crossing angle. By the end of the fill, it can be as small as 240 μ rad.

The instantaneous luminosity can be increased by the inclusion of more bunches in the beam, decreasing the size of the beam through improved quadrupole magnets, and by reducing

²Add the H factor from the hourglass effect and explain?

³Add mathematical formula for F?

the crossing angle. Tuning these parameters led the LHC to reach its design luminosity of $10^{34} \text{ cm}^{-2} \text{ s}^{-1}$ in 2016. It had more than doubled by the end of Run-2.

Integrating the instantaneous luminosity over a period of time yields the *integrated luminosity* $\mathcal{L}_{\text{int.}}$:

$$(3.3) \quad \mathcal{L}_{\text{int.}} = \int \mathcal{L} dt$$

These values are often quoted by experiments in units of “inverse femtobarn” (fb^{-1}) as an indicator of the amount of collision data collected. A “barn” is a unit equal to 10^{-28} m^2 and colloquially used to express cross sectional area in nuclear and particle physics. Thus its reciprocal, the same units as integrated luminosity, gives a good sense of scale that relates cross sections of individual processes to the total amount of data. Tab. 3.1 gives the integrated luminosities over Run-2 delivered by the LHC and collected by CMS. Taking 137.19 fb^{-1} from this table, and assuming the inelastic p_T cross section above gives an estimate of 10^{16} collisions recorded by CMS over Run-2 (excluding pileup interactions).

3.2.3 Pileup

At the high instantaneous luminosity of the LHC, multiple interactions per bunch crossing (known as *pileup*) are frequent. The expected, or nominal, number of collisions per bunch crossing is one, but because of all the factors that increase the luminosity, many “softer” collisions also take place. Pileup interactions can produce many low- p_T objects, and near-collinear to the beam (detecting particles in this region is essential for some analyses). These additional objects can contaminate the reconstruction of final state from the nominal collision, and as such affect the direction and magnitude of the p_T^{miss} . When one aims to increase the luminosity to collect more data, the more severe pollution from pileup is an inevitable consequence. The distribution of pileup events in CMS during Run-2 can be seen in Fig. 3.2.

There are strategies in place in the LHC and the anchored experiments to mitigate pileup. Introducing, or increasing, a crossing angle between the beams reduces the effect. Track reconstruction algorithms are very efficient at connecting particles to their primary vertices, and therefore particles originating from pileup vertices can be identified and removed [2, 37]. At CMS, various methods are available in the calorimeter triggers to subtract the [effects] from pileup.

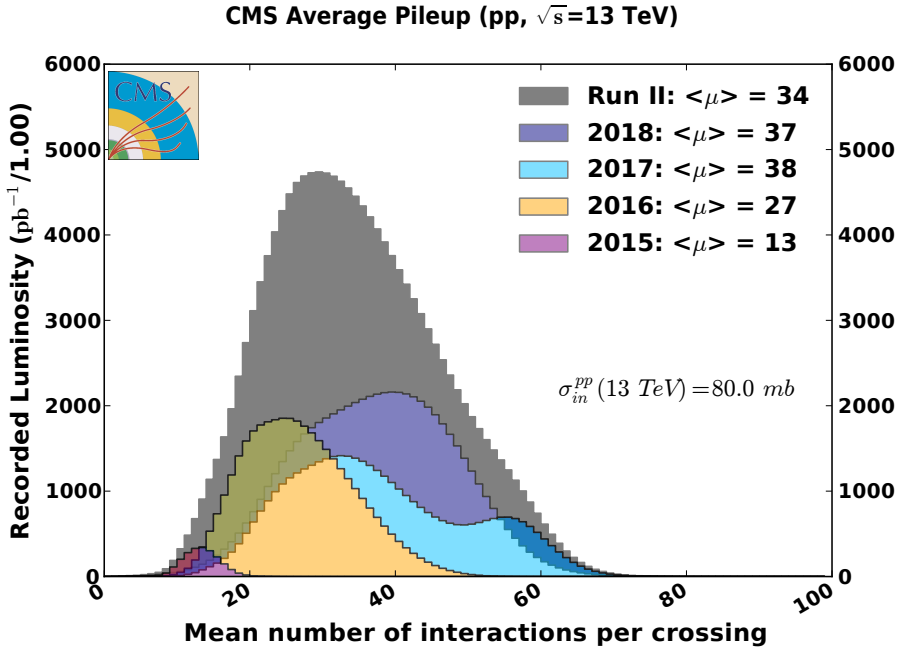


Figure 3.2: The average number of pileup interactions at CMS during 2015 and Run-2 of the LHC. Figure obtained from Ref. 43.

3.2.4 Evolution of the LHC

The LHC began operating in 2010 at a centre of mass energy of $\sqrt{s} = 7 \text{ TeV}$, 3.5 TeV per beam. A modest increase to 8 TeV was achieved by the end of Run-1 in 2013. Long Shutdown 1 then commenced where maintenance work was carried out, and upgrades to the accelerator and experiments were performed. Notably, the superconducting magnets were improved to safely handle much more energetic beams.

The LHC resumed operation in 2015, marking the start of Run-2 and further pushing the frontiers of high energy physics with a centre of mass energy of $\sqrt{s} = 13 \text{ TeV}$. While valuable data was taken that year, it was not until 2016 when substantial datasets were amassed. Therefore, when analysts refer to the “full Run-2 dataset”, they typically do not include data from 2015. It requires as much care as the other years with respect to implementing corrections and addressing systematic uncertainties, and so on, for only a very small gain in integrated luminosity. Run-2 ended in 2018 with — omitting the 2015 dataset — 158.64 fb^{-1} of pp collisions delivered, 146.45 fb^{-1} of which were recorded by CMS who certified 137.19 fb^{-1} suitable for analysis [43, 44]. A breakdown by year is presented in Tab. 3.1 with a visual representation in Fig. 3.3.

In addition to the upgrades that have so far been performed, a much grander change is on

Integrated luminosity	2015	2016	2017	2018	Full Run-2
Delivered by LHC (fb^{-1})	4.21	40.99	49.79	67.86	162.85
Recorded by CMS (fb^{-1})	3.80	37.80	44.98	63.67	150.25
Certified by CMS (fb^{-1})	2.26	35.92	41.53	59.74	139.45

Table 3.1: The integrated luminosity delivered by the LHC during Run-2 which were recorded and certified by CMS. Typically, only the 2016–18 datasets are analysed since 2015 accrued little data compared to the other years. Numbers obtained from Refs. 43, 44.

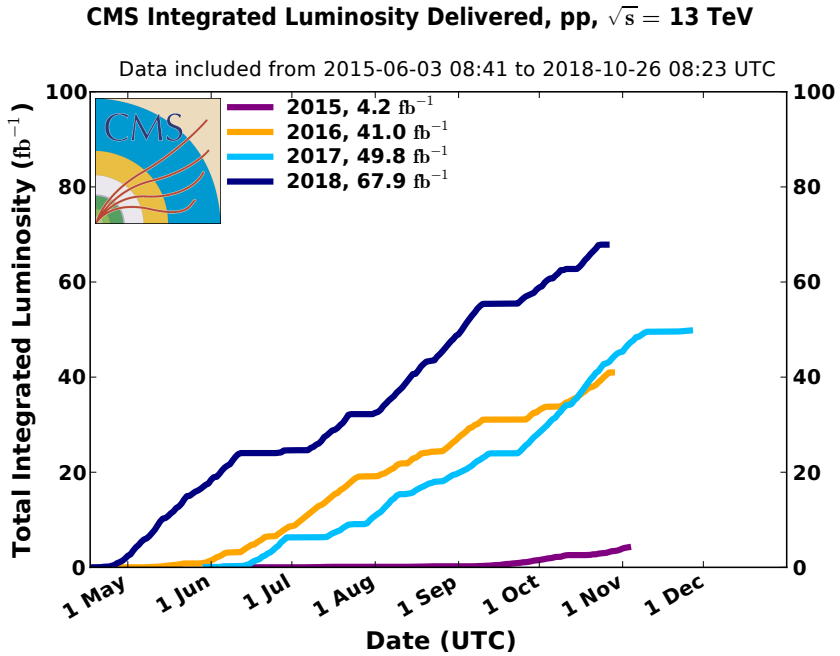


Figure 3.3: The integrated luminosity of pp collision data delivered to CMS during Run-2 of the LHC. Figure obtained from Ref. 43.

the horizon. In 2027, the High Luminosity Large Hadron Collider (HL-LHC) is expected to begin operations. The latest technical design report can be found at Ref. 15. Many [upgrades] are set to be introduced with the primary purpose of increasing the luminosity by up to a factor of ten: more powerful magnets for focusing the beam, crab cavities for increasing the bunch overlap area, shielding and more radiation-resistant components, an upgrade to many of the boosters in the accelerator complex, and much more. A summary of the important parameters at three stages of the LHC’s life is given in Tab. 3.2.

Parameter	End of Run-2	HL-LHC	Design
Beam energy (TeV)	6.5	7	7
Bunches per beam	2,556	2,748	2,808
Protons per bunch	1.5×10^{11}	2.2×10^{11}	1.5×10^{11}
Crossing angle (μrad)	300	590	285
Instantaneous luminosity ($\text{cm}^{-2}\text{s}^{-1}$)	2.1×10^{34}	7.2×10^{34} *	1.0×10^{34}
Integrated luminosity per year (fb^{-1})	68	250	40
Average pileup per bunch crossing	34	140	27

Table 3.2: Some of the important parameters defining the performance of the LHC at the end of Run-2, for the High Luminosity Large Hadron Collider and the design specification. Several values in this table were obtained from Refs. 14, 27.

* Does not account for the large increase to virtual luminosity from the introduction of crab cavities.

3.3 The CMS experiment

The Compact Muon Solenoid (CMS) collaboration was formed in 1992 with a letter of intent circulated to the high energy physics community for a general purpose detector to be built at the LHC [52]. Though its emphasis was the detection of the Higgs boson, the myriad avenues for which physics could be studied was also acknowledged. Just under five hundred people from sixty two institutes were part of the original letter. At the time of writing over five thousand physicists, engineers, technical and administrative staff, and students, spanning over two hundred institutes in fifty countries, comprise the collaboration. Working tirelessly in harmony, with ingenuity, cooperation, and a drive for exploring the frontiers of particle physics, almost one thousand publications have been produced with data collected by the experiment. These range from exotic/BSM searches, standard model precision measurements, B -physics, top quark physics, heavy ions, and more. This wide scope of topics cements CMS as a versatile and world-leading detector, and collaboration as a whole.

3.3.1 The CMS detector

The machine, aptly named the “CMS detector”, lives a hundred metres underground at Interaction Point 5, just outside the town of Cessy in France. Constructed over several years, the detector construction of the detector was separated into fifteen sections. Each was built on the surface and lowered into the experimental cavern with an incredibly small tolerance of a few centimetres. Here, they were joined together to assemble the 14,000 tonne goliath. The finished detector is a hermetic cylinder enclosing the LHC beam pipe, measuring 21 m in length (plus a little extra from the smaller, bolt-on forward calorimeters) and 15 m in

diameter. Its etymology stems from how *compact* (relatively speaking) the detector is as it weighs twice as much as ATLAS in only one sixth of the volume, it has a subsystem dedicated to detecting *muons*, and a *solenoid* is used to generate the magnetic field.

CMS is designed to detect all manner of particles as accurately as possible. To accomplish this, the detector can be divided into four subsystems (or subdetectors): the silicon tracker, the electromagnetic calorimeter (ECAL), the hadron calorimeter (HCAL), and the muon chambers. These are each explained in more detail below, with a graphic of the entire detector presented in Fig. 3.4 and a transverse slice through it in Fig. 3.5.

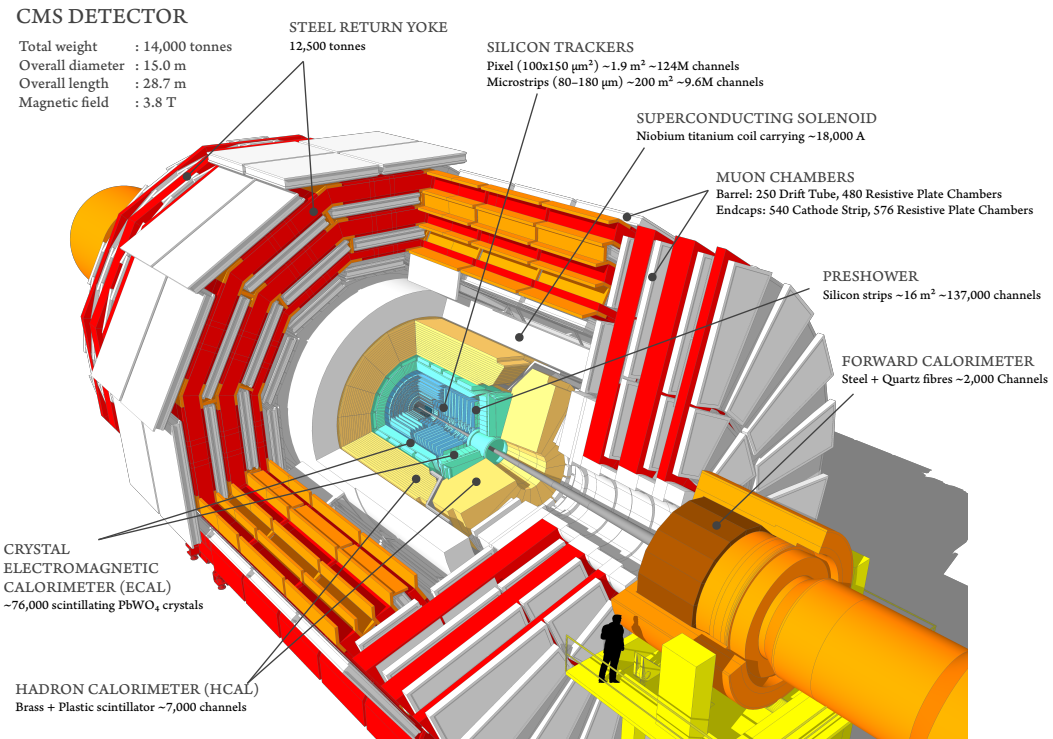


Figure 3.4: A cutaway diagram of the CMS detector with all of the principal components labelled. This detector configuration was used for the 2017–18 data taking years, where the coverage of the pixel detectors in the silicon tracker were upgraded from 1 m^2 (66 million channels) to 1.9 m^2 (124 million channels). Image taken from Ref. 91.

3.3.1.1 Subsystems

When a collision occurs, the ejected particles first encounter the silicon tracker that extends from 4 cm to just under 1 m in radius [49, 78]. Consisting of tens of millions of pixels and microstrips, the positions of particles can be recorded to within $10 \mu\text{m}$. Initially, the pixel detector covered 1 m^2 , consisting of 66 million channels. It was upgraded for the 2017–18 run

period to 1.9 m^2 with 124 million channels. Since it is the closest subsystem to the interaction point, the components must be extremely radiation tolerant to withstand the bombardment of particles pummelling them every collision.

After the tracker, the particles can interact with the ECAL [30, 46]. The 76,000 lead-tungstate crystals record energy deposits in the barrel and end cap regions belonging to charged particles. In particular, electrons and photons are identified here, and are usually stopped entirely in the ECAL.

Hadronic particles can propagate further into the HCAL [47]. A brass and plastic scintillator with 7,000 channels, the energies in showers of hadrons are measured. Unlike the ECAL which only covers the barrel and end cap, the HCAL also has a component in the forward region of the detector: the hadron forward calorimeter (HF). Made of quartz fibres and steel, it is designed for particles with trajectories close to the beam line, and serves the additional function of measuring the luminosity delivered to, and collected by, the experiment. Each cell of the HCAL maps onto a given number of ECAL crystals, forming “calorimeter towers” that are important when collecting data (see Chpt. 3.3.2). The towers project mostly radially from the interaction point. Their granularity is greatest perpendicular to the beam line, and decreases closer to it.

These three subsystems are encased in a massive solenoid [48], making up 12,500 of the 14,000 tonne detector. It generates a magnetic field of 3.8 T and $2.4 \times 10^9 \text{ J}$ of energy, making it the largest store of energy in the world for a single magnet. The field allows for the transverse momentum of a charged particle to be measured at high resolution, since it deflects the particle into a circular orbit. The magnetic force qvB exerted is equal to the centripetal force mv^2/r , and therefore the radius of the orbit is proportional to the momentum.

An iron return yoke interspersed with the muon chambers [83] [make up] the rest of the detector, extending from a radius of around 3 m to 7.5 m . The iron yoke confines the magnetic field to the volume of the detector and provides a 2 T field in the opposite direction to that found further inward. Since muons are much heavier than electrons and have high p_T , they deposit little energy in the ECAL. The final states of several interesting decays, such as the Higgs, that produce muons. Consequently, constructing a dedicated subdetector is therefore essential. There are four muon “stations”, as can be seen by the orange strips in Fig. 3.5, separated by portions of the return yoke. 480 resistive plate chambers and 250 drift tubes reside in the barrel region, with 540 cathode strip chambers complemented by 576 resistive plate chambers in the end caps.

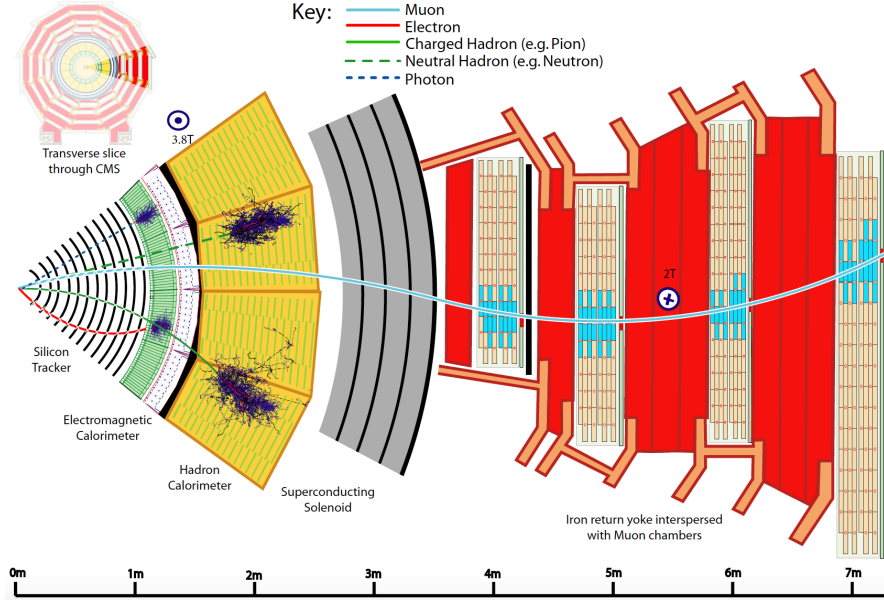


Figure 3.5: A transverse slice through the CMS detector with the main subsystems and components visible (figure obtained from Ref. 94). Several particles produced at the primary vertex and their interactions with the detector are also depicted.

3.3.1.2 Geometry

Collider physics tends to use certain conventions when describing the positions of particles in a detector. The azimuthal angle ϕ is the same variable as in cylindrical coordinates, i.e., the angle between the particle's position and the longitudinal axis of the detector (the beam line). Pseudorapidity, denoted by η , is a coordinate that describes the angle of a particle (after a collision in an accelerator) relative to the beam axis:

$$(3.4) \quad \eta = -\ln \left[\tan \left(\frac{\theta}{2} \right) \right]$$

where θ is the angle between the particle's three-momentum \mathbf{p} and the positive direction of the beam axis. So as $\theta \rightarrow 0^\circ$ (the beam line), $\eta \rightarrow \infty$. Generally, particles with large η escape the detector which is why forward calorimeters are in place. The transverse momentum of a particle can be found with $p_T = |\mathbf{p}| / \cosh \eta$.

The subdetectors of CMS are nominally separated into several sections dependent on their geometry, and can mostly be divided into η ranges. In the ECAL and HCAL, the barrel region corresponds to $|\eta| < 1.479$ and the end cap region $1.479 < |\eta| < 2.964$. The HF occupies $2.964 < |\eta| < 5.191$. These boundaries are defined by the edges of the calorimeter towers. The tracker extends out to $|\eta| < 2.5$, known as the “central region”. Its barrel and

end cap sections are bound by $|\eta| \lesssim 1.6$ and $1.6 \lesssim |\eta| 2.5$, respectively. The muon chambers comprise of a central barrel region ($|\eta| < 1.1$) and central end cap region ($0.9|\eta| < 2.4$). It overlaps with the barrel since the components are designed parallel and perpendicular to the beam line, not according to η . The pseudorapidity range of the muon chambers' end cap is restricted compared to the ECAL and HCAL because of the bounds of the tracker, and the steel that surrounds the structure takes up the remainder of the end cap. One quadrant of CMS showing the η divisions can be seen in Fig. 3.6.

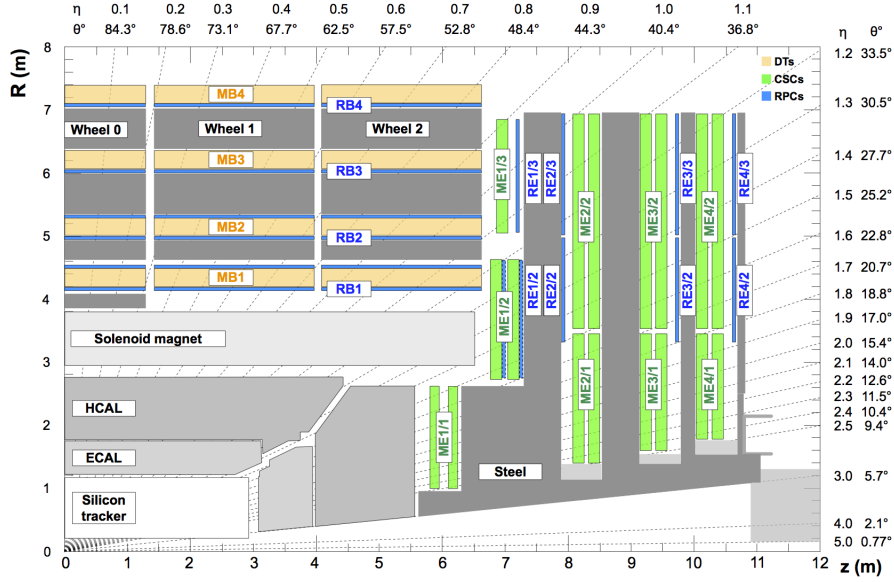


Figure 3.6: A quadrant of the CMS detector showing the main subsystems with their radius R , longitudinal distance z , and pseudorapidity η from the interaction point. The grey box at $3 < |\eta| < 5$ and $11 < z < 12$ m is the hadron forward calorimeter. Figure taken from Ref. 87.

The distance between two objects can be found with the variable ΔR :

$$(3.5) \quad \Delta R = \sqrt{(\Delta\eta)^2 + (\Delta\phi)^2}$$

It is often used as a distance parameter in jet clustering, or between individual objects in highly-boosted decays.

3.3.2 Data acquisition and triggering

With the enormous collision rate at the CMS interaction point, acquiring data requires some thought and ingenuity. Today's electronics cannot handle the bandwidth from recording

every single collision, $\mathcal{O}(1 \text{ petabyte s}^{-1})$. As such, a “trigger” is used to select the events that may be of use to analysers. In CMS, a two stage trigger [25] is used: the Level-1 Trigger (L1T), implemented in the detector hardware; and the High-Level Trigger (HLT) [39], a software farm to further reduce the events selected at Level-1. The trigger is part of the larger data acquisition (DAQ) system, an intricate network of custom electronics and commercial processors — a union of hardware, firmware, and software — interconnected by multi-gigabit links to record the products of the highest-energy manmade collisions on Earth.

3.3.2.1 The Level-1 Trigger

The Level-1 Trigger is a set of algorithms (a trigger “menu”)⁴ implemented in custom hardware designed to reduce the event rate from 40 MHz to a maximum of 100 kHz. FPGA and ASIC chips contain the algorithms in firmware, with timing systems synchronised with the LHC clock. When a collision occurs, particles interact with the detector and registered by the components.

Coarsely-segmented data is sent from the ECAL and HCAL through a two-layer Calorimeter Trigger. These are arrays of custom processors located at Point 5. Layer-1 receives data from the calorimeters over upwards of one thousand fibre optic links, each with multi-gigabit bandwidths. The information from the two subsystems are combined into calorimeter towers, and some simple position- and energy-dependent calibrations are applied.⁵ The data from Layer-1 is then transmitted to Layer-2, again over many high-bandwidth optical links. Here, physics object candidates are identified (jets, e , γ , τ).⁶ Additional calibrations are applied to them (for example, in Chpt. 3.3.4), and simple pileup subtraction is performed.⁷ Energy sums are also calculated at this stage, such as E_T^{miss} , H_T , and H_T^{miss} .

In parallel, the various subdetectors in the muon chambers pass information through successive stages, notably the Muon Track-Finder Layer (EXPAND), and is then combined with some of the calorimeter information in a sorting/merging/isolation layer. The output from this layer is combined with the remaining information in Layer-2 in the Global Trigger, a series of μ TCA boards with FPGAs. The trigger menu lives here, and all of the information gathered — object candidates, energy sums, beam conditions — is provided to it. These triggers may be dependent on the presence a single object or the number of objects of a single

⁴Do I need to say that different menus are used throughout the data-taking periods and for different injectants (heavy ions, etc.)?

⁵Mention something about trigger primitives here?

⁶An overview of the latest Run-2 algorithms for object identification can be found in Ref. 107.

⁷Do I need to describe in detail how jets are formed? Jet seed, chunky donut PU subtraction, etc... Since it may be relevant for JEC.

class (e.g., one muon, two jets), multiple classes of object (cross triggers), the energy sums, the topologies of objects, and more. The latency given to make a decision on whether to keep or reject an event is 4 μs .⁸ A diagram of this data flow is given in Fig. 3.7.

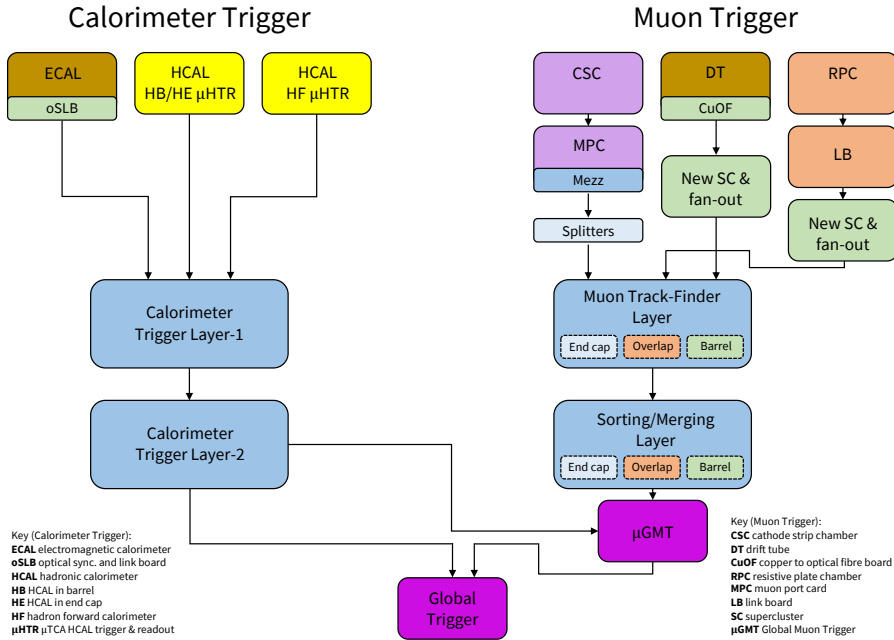


Figure 3.7: A summary of the CMS Level-1 Trigger data flow from the hits recorded by the subsystems to the Global Trigger. Figure reproduced from Ref. [53].

A small subset of data from the L1T is diverted for monitoring purposes. During data taking periods, CMS has a plethora of members that participate in the maintenance and observation of the experiment. At Point 5, shifters monitor the different [areas] collecting information from various sources. Data acquisition, data quality, access to the experimental cavern, the L1T (which I have performed on numerous occasions), and the HLT are among them. Experts in these, and more specific, systems are on call on a rotating period. I, myself, have been an on call for Layer-2 of the Calorimeter Trigger several times.

3.3.2.2 The High-Level Trigger

Events that pass a logical OR of the triggers at Level-1 are transmitted to the HLT. The higher resolution data collected at the point of collision is available, along with information from the tracker. Populated with Intel Xeon processors (high core count CPUs), approximately 22,000 cores are available (by the end of Run-2) to process the data sent from the L1T. In order

⁸Mention pre-scaling of triggers, and that as \mathcal{L} decreases over a fill, the pre-scales change?

to avoid a back-log, a 100 kHz input rate allows a HLT node \sim 220 ms to make a decision. High-level software in the cmssw environment (written in C++ and Python, see Chpt. [REF]) is executed. A larger and more complex trigger menu is available, including the possibility analysis-specific triggers (such as those that target VBF topologies in Chpt. 4). Complex variables such as α_T can even be calculated and triggered on.

Physics objects are reconstructed further, with algorithms such as anti- k_T algorithm used to cluster jets [34]. Additional classification algorithms are also applied to objects, such as the DEEPCSV neural network to identify b -jets. Some of these algorithms can be computationally expensive. Consequently, approximations/parameterisations are used at HLT level. A global event reconstruction from the PARTICLE FLOW algorithm (PF) [45, 94] is performed as well. The [fully-fledged] versions of these kind of algorithms are re-run on the retained events in later stages of postprocessing.

The HLT reduces the event rate from the maximum 100 kHz input substantially down to around 1 kHz. The datastream $\mathcal{O}(6 \text{ GB s}^{-1})$ is then subject to further processing before the analysts access it. As well as the data being stored on networked hard drives at sites across the globe, back ups are made to magnetic tape for long term storage. As with the Level-1 Trigger, some data is [diverted] for monitoring, object calibrations, and alignment of detector components.

3.3.3 Simulating CMS data

Data recorded by CMS is paramount for analyses searching for new physics. However, simulated samples are also of high importance. Events for specific processes are generated using Monte Carlo (MC) random sampling, and the output datasets are often collectively referred to by the method: “Monte Carlo” or “MC”. The datasets are often generated with large numbers of events to minimise the associated statistical uncertainty. MC samples are useful in a variety of cases: understanding the kinematics of signal processes in searches for new physics, modelling background processes that can mimic signal, and comparisons to data for validation purposes.

A matrix element generator such as MADGRAPH [13] or POWHEG [62, 89] models the hard scattering process, usually at leading order (LO) but sometimes at higher orders. Events then pass through a hadroniser (usually PYTHIA [99] in CMS) to model hadronisation of quarks and gluons, sometimes known as the *parton shower* – the softer radiation that accompanies the hard scatter. Jets are clustered here by, for example, the anti- k_T algorithm. The particles are also run through a detector simulation that emulates the configuration and response of the detector in different years. Material interactions and emulation of the triggers are

included. GEANT4 [9, 11, 12] provides this in CMS. Once the particles have been appropriately simulated, they are given the same postprocessing treatment as actual data, such as executing object tagging algorithms so that the data and simulated samples are as comparable as possible.

3.3.4 Jet energy corrections in the Level-1 Trigger

Recording the properties of hadrons that are amalgamated into jets is not always consistent across the detector. While the components go through quality control, there is inevitably some variation in their performance. They can degrade at different rates. Some may also receive hits more often than others and be subject to greater radiation damage. As a result, non-uniformity of the detector response — parameterised in terms of p_T and η — must be compensated for. For jets, this comes in the form of jet energy corrections (JEC).

As outlined in Chpt. 3.3.2.1, the trigger primitives from the ECAL and HCAL enter Layer-1 of the Calorimeter Trigger and coarse position- and energy-dependent calibrations are applied. jets as objects are initially identified in Layer-2, and preliminary calibrations correct their energy. Disregarding these, even at this early stage in the data acquisition workflow, can affect the efficiency and rate of the Level-1 Trigger. It is therefore important to re-derive the calibrations regularly, since the configuration of the detector and beam conditions change over the lifetime of the experiment.

When a new round of calibrations are derived, there are many steps before this one. Preceding it, Layer-1 experts calculate their scale factors for the calorimeter towers. Once performed, the jet energy corrections are then derived in CMSSW.

3.3.4.1 The procedure

QCD multijet MC datasets with a large p_T range used to derive the Layer-1 and Layer-2 calibrations. Corresponding jets in data for this process are often mismeasured (so providing good calibrations in the most difficult scenario is a good test), and MC events contain “truth-level” information from the generator. Ntuples are made from these which have the Layer-1 corrections applied. Referring to the processing chain in Chpt. 3.3.3, the jets these calibrations are derived for are post-hadronisation, but before interaction with the detector. They will be referred to as “Level-1 (L1) jets”. The reference jets directly from the generator (“GenJets” as colloquialised in CMS) are important for matching to our L1 jets to ensure we are not mistakenly using jets [birthed] in the parton shower that have no reference point.

The reference and L1 jets are matched using the variable ΔR (see Eq. 3.5). The algorithm used to match the jets does so by inspecting each L1 jet in descending p_T and searching for

a reference jet with $\Delta R < 0.25$. If there is more than one match, the reference jet with the smallest ΔR is taken. Then the next L1 jet (and so on) follows the same procedure, with the previous reference jet removed from the matching collection.

The pairs of jets are categorised into sixteen bins of $|\eta|$, the highest granularity available since the calibrations must run quickly on hardware. Each in is then analysed in turn.

Within each $|\eta|$ bin, the jet pairs are subdivided into bins of the transverse momentum of the reference jet ($p_T^{\text{ref.}}$). The bin widths, like $|\eta|$, are variable. The ratio of the transverse momentum of the L1 jet (p_T^{L1}) to $p_T^{\text{ref.}}$ is taken for each pair of jets. Our metric for measuring the detector response is the mean of these ratios:

$$(3.6) \quad r_j = \langle p_T^{\text{L1}} / p_T^{\text{ref.}} \rangle$$

The reciprocal of the r_j vs. p_T^{L1} is inspected and a correction curve is fitted. A gaussian captures the peak at low p_T and the following equation⁹ is used for the tail:

$$(3.7) \quad p_T^{\text{L1, corr.}} = p_T^{\text{L1}} \cdot \left(p_0 + \frac{p_1}{\left(\log_{10} p_T^{\text{L1}} \right)^2 + p_2} + p_3 \cdot \exp \left(-p_4 \left(\log_{10} p_T^{\text{L1}} - p_5 \right)^2 \right) \right)$$

The input parameters for the function may not be adequate, so they are tuned to capture the low- p_T spike and high- p_T plateau (see Fig. 3.8 for a visual representation). The value of this fit function in each $p_T^{\text{ref.}}$ bin is exported.

Once all $|\eta|$ bins have been inspected, the calibrations are consolidated in several forms. A machine-readable lookup table is [put] in the firmware of the Layer-2 hardware, so that the corrections are applied in the trigger. A version is added to the Level-1 Trigger packages in CMSSW so that the next steps in the calibration chain can utilise them.

A closure test is conducted to validate the corrections we have just produced. The MC ntuples are regenerated with the JEC applied. Jet matching is performed and the calibrations are checked. Many diagnostic and performance plots are produced to ensure the calibrations are [performing] as expected. These can be inclusive of the number of pileup interactions, or split into ranges to see if the calibrations differ between them. Examples of these are Fig. 3.9 showing scatter plots of $p_T^{\text{ref.}}$ vs. p_T^{L1} before and after JEC are applied, and Fig. 3.10 shows the response.

⁹Go into more detail regarding the equation? Reasoning, etc.

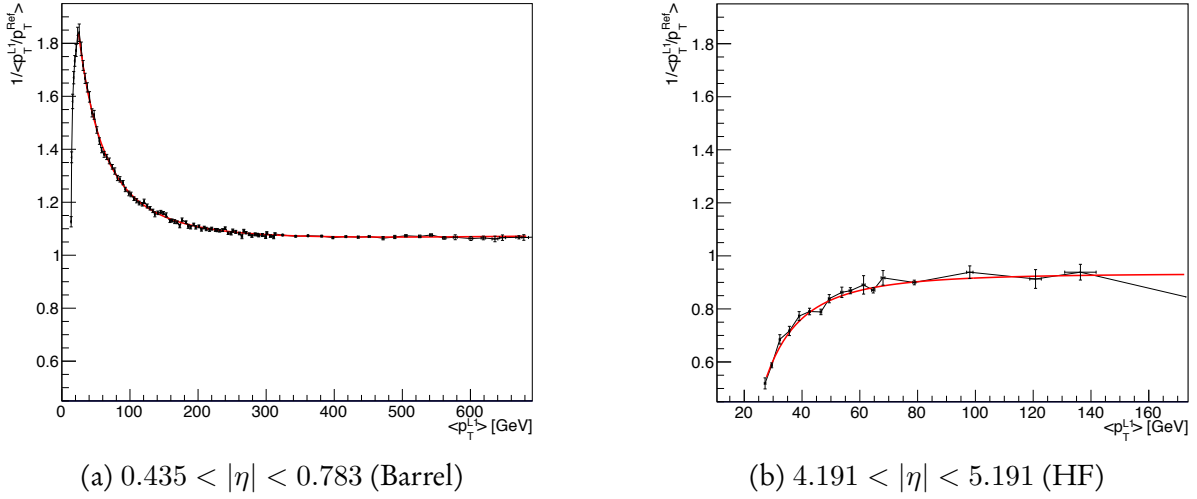


Figure 3.8: Examples of correction curves used to calibrate the jet energies in two $|\eta|$ bins. The reciprocal of the response is plotted against the p_T of the Level-1 jet, and a complex function (Eq. 3.6) fits the points. These plots are from the jet energy corrections performed on 2018 QCD Monte Carlo.

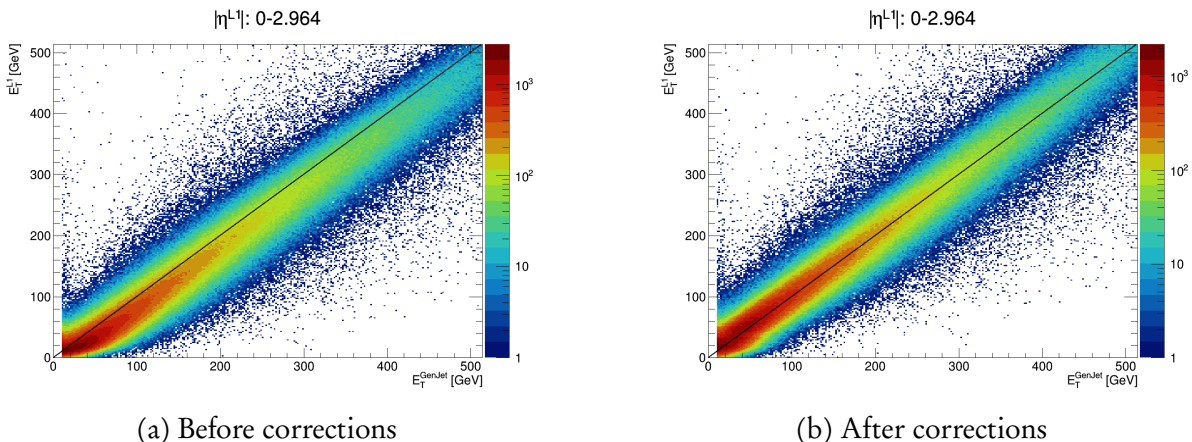


Figure 3.9: The energies of matched pairs of jets in the entire barrel and end cap, in the pileup 40–50 range, before and after jet energy corrections have been applied. After calibrations, the distribution is much more symmetrical. An equivalent plot using jets from LHC data is expected to look similar after applying these calibrations.

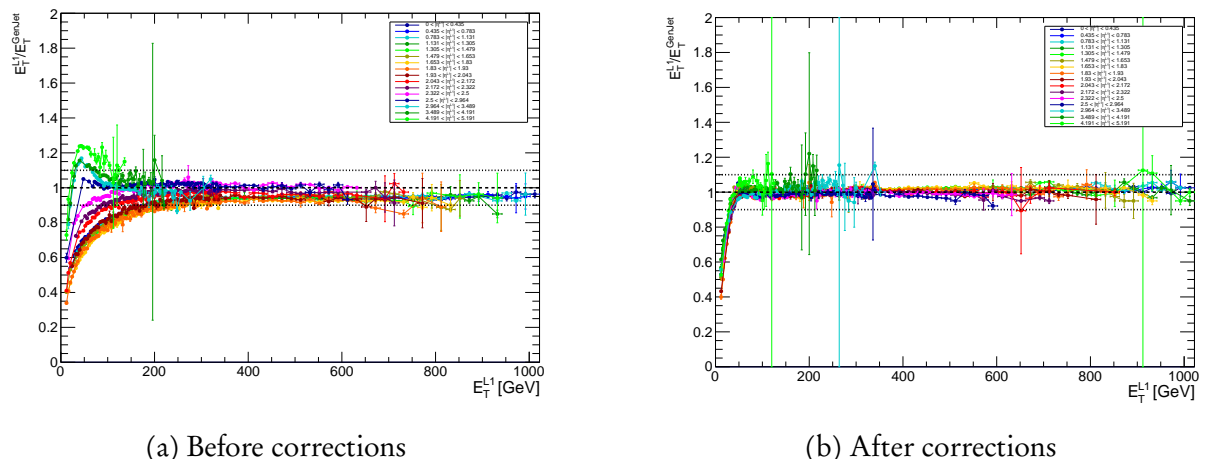


Figure 3.10: The response curves in each $|\eta|$ bin as a function of p_T^{L1} , in the pileup 40–50 range, before and after JEC are applied. Note that in panel b, the x -axis is the corrected p_T^{L1} .

COMBINED SEARCH FOR INVISIBLY DECAYING HIGGS BOSONS IN HADRONIC CHANNELS

This is the analysis chapter on $H \rightarrow \text{inv.}$.

- Discuss how the theoretical aspects from the Theory chapter translate into an experimental search.

- Discuss the necessity of including all production modes of Higgs (invisible final state, so characterise events based on initial/additional particles). Also mention how sensitive each production mode is at contributing to the branching ratio limit. Emphasise the non-VBF modes (ggF , $t\bar{t}H$, $VH - W^+H$, W^-H , ZH) in this chapter as that's what I've been working on and another student will be covering VBF.
- Add a section or subsection somewhere regarding analysis tools. Perhaps add a brief description of ROOT (and how it's entrenched in HEP even though people are tending to move away from ROOT-based analysis onto more industry-standard tools), then lead into the FAST tools and using dataframes, vectorisation, etc., with only small interfaces to ROOT (for I/O) to extract data. Potentially mention how the data tiers work in CMS (RAW, DIGI, RECO, AOD, miniAOD, nanoAOD, etc.)
- Talk about what makes this analysis unique: doing a combination over all production modes from the start instead of separate analyses combined at the end. Means we can share samples, systematics, background methods and workflows, build in orthogonality between the different modes and cover as much phase space as possible (with new final states such as boosted Z bosons with unresolved subjects). This makes the analysis much

more cohesive and consistent.

- Include object definitions, overall analysis strategy, triggers, signal production (with each non-VBF mode in detail), event selection, background estimation (control regions, sidebands) and results/limit (including comparisons to previous results).
- Emphasise my contributions: control region construction and studies, background estimation, and other studies I will have conducted by the time I write up.
- Current material: no public plots as of yet. Hope to finish analysis by the time I begin writing up. We are preparing a CMS internal analysis note, documenting all aspects of the analysis. I will add all relevant information there which I can subsequently use when writing this chapter.
- Since it's my thesis, I can talk about $t\bar{t}H$, VH and ggF /monojet, even though the Bristol contribution to the final, public result would only be $t\bar{t}H$ and resolved VH . Would need to be able to run the fit for all three modes simultaneously, ensuring we have complete (and correct) systematics for ggF .

4.1 Analysis overview

4.1.1 Hadronic production modes of the Higgs boson

4.2 Categorisation of the non-VBF production modes

4.3 Data and simulation

4.3.1 Weights and corrections for simulated processes

In order for simulated events, particularly for background processes, to resemble LHC data as closely as possible, many corrections and weights are applied. These are discussed in more detail in the following sections [REF]. A final event weight w_{event} is the product of the weights from all of the individual sources i that provide a weight:

$$(4.1) \quad w_{\text{event}} = \prod_i w_i$$

When representing these events in histograms, the yield in a given bin $N_{\text{corr.}}$ is the sum of these event weights:

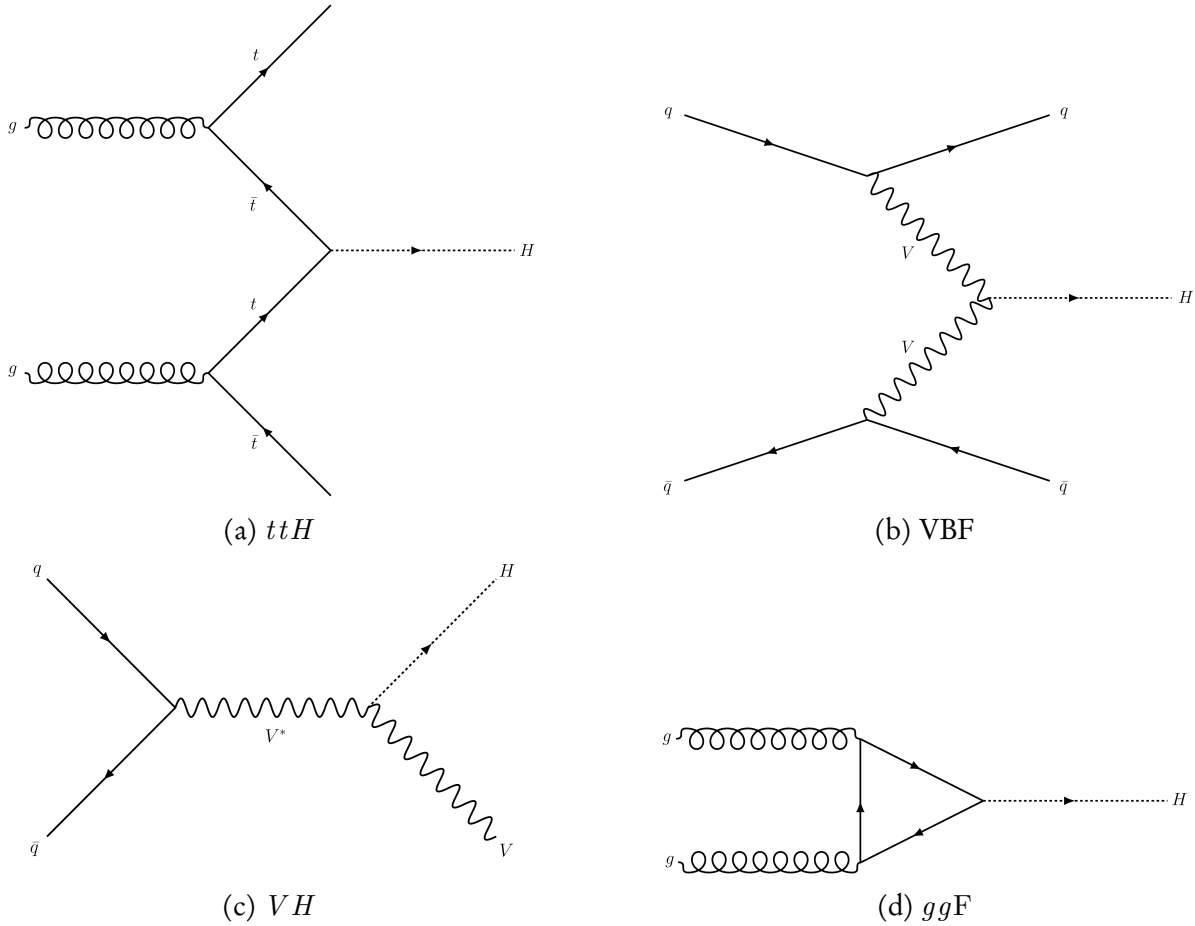


Figure 4.1: The Feynman diagrams for the four main hadronic production modes of the Higgs boson.

$$(4.2) \quad N_{\text{corr.}} = \sum_j^{N_{\text{MC}}} w_{\text{event } j}$$

where N_{MC} is the number of unweighted simulated events in the bin. The statistical uncertainty ascribed to the yield in a bin is given as

$$(4.3) \quad \Delta N_{\text{corr.}} = \pm \frac{N_{\text{corr.}}}{\sqrt{N_{\text{MC}}}}$$

The statistical uncertainty for the number of events in data is simply the Poissonian error

$$(4.4) \quad \Delta N_{\text{data}} = \pm \frac{N_{\text{data}}}{\sqrt{N_{\text{data}}}}$$

The standard prescription for error propagation is to approximate the uncertainty as the square root of the sum of the weights squared [28]:

$$(4.5) \quad \Delta N_{\text{corr.}} = \pm \left(\sum_j^{N_{\text{MC}}} w_{\text{event } j}^2 \right)^{1/2}$$

Our reasoning for using Eq. 4.3 instead of Eq. 4.5 is that the error should be determined purely from the integer number of events we select (k in a Poisson statistical treatment), regardless of whether they are weighted or not. This often reduces the uncertainty for MC compared to Eq. 4.5 since many more events are generated to predict a given equivalent luminosity. Further justification is that it is a good approximation in our assumed regime where we expect a large number of events from our MC samples before any cuts are applied (say N), and a large enough number of events after the cuts such that we do not encounter the low- k or low- N limits of Poissonian error propagation.

4.3.1.1 Cross section reweighting

Since an arbitrary number of events can be generated for simulation, and a larger number of events gives higher statistical power, events in these datasets need to be reweighted to normalise their contribution to a given region or category. To first order, the weight applied is

$$(4.6) \quad w_\sigma = \frac{\sigma \mathcal{L}_{\text{int.}}}{N \varepsilon}$$

where σ is the cross section of the process at the order it was generated (e.g., on DAS/XSDB for public datasets), $\mathcal{L}_{\text{int.}}$ is the integrated luminosity of the LHC data it is being compared to, N is the number of events in the dataset before any skimming (or the sum of the generator weights), and ε is the filter efficiency (assumed to be unity for all datasets since no generator-level cuts are applied). If a dataset is generated at leading order, higher order corrections are usually applied on an event-by-event basis that changes the shapes of distributions (see [SEC ON NLO CORRECTIONS]). In some circumstances, “flat” k-factors can be applied to a dataset that only alters the normalisation (i.e., its cross section).

4.3.1.2 Pileup

Pileup interactions at the LHC are frequent (see Chpt. 3.2.3) and must be modelled appropriately in simulation. Simulated samples are generated with a certain distribution of the

number of pileup interactions which usually does not match the data recorded by CMS. This is due to changing conditions in the beam over a period of data taking. In order to make them comparable, the simulated events are reweighted; in this context it is known as *pileup reweighting*. ROOT files containing histograms of the number of pileup interactions from short runs in the LHC are available centrally and are used as the reference for which to reweight the simulated events.

In the trees of the simulated samples, the branch `Pileup_nTrueInt` is the mean of the Poisson distribution from which random numbers are drawn. In each simulated event, these random numbers (all from the same distribution) are used to set the number of in-time pileup interactions as well as the number of the interactions in each neighbouring bunch crossing to simulate the out-of-time pileup. In data, the same branch gives the average number of pileup interactions for a colliding bunch pair in a lumi section. The distribution of `Pileup_nTrueInt` in the data is derived from the measured instantaneous luminosity for each colliding bunch pair in each lumi section and the cross section of the total inelastic $p\bar{p}$ interaction.

The nominal pileup weight for each simulated event, as well as the up and down systematic variations, are derived in NANOAOD-TOOLS.

4.3.1.3 Veto and selection weights

In an analysis, events are often rejected by placing kinematic or object-based requirements. This type of selection strictly removes an event from the analysis if the requirement is not met. While kinematic requirements are either fulfilled or not, a different approach can be used when selecting the number of objects, i.e., when defining control regions. For a set of objects, the selection weight at event level is defined as

$$(4.7) \quad w_{\text{sel.}} = \prod_i^{N_{\text{objects}}} \epsilon_i$$

where ϵ_i is the efficiency/scale factor applied to object i . Only reconstructed (“reco” level) objects that have been matched to a generator level object are considered. For leptons (e, μ, τ) and photons, these scale factors are typically from the reconstruction efficiency, identification efficiency, and p_T - or η -dependent energy corrections. In the case of b -tagged jets, it is the data-MC scale factor at the given working point of the algorithm used to identify them. These weights are calculated individually for each type of object in an event, and individually for each source since they also introduce systematic variations that cannot be trivially aggregated. A veto weight is defined as

$$(4.8) \quad w_{\text{veto}} = \prod_i^{N_{\text{objects}}} 1 - \epsilon_i$$

The uncertainties/systematic variations follow the same prescription. With these quantities defined, an event that meets the object criteria is given the selection weight, otherwise it is given the veto weight. For example, if an event with one muon that meets the criteria for the $\mu + \text{jets}$ region will enter that region with its selection weight. That same event can also enter the signal region or one of the sidebands (depending on the event kinematics) with the veto weights. This “migration” of events, where they are able to contribute to more than one region, and the fact that weights are applied instead of event rejection, provides a noticeable decrease to the Monte Carlo statistical uncertainty in a given bin of a given distribution.

One thing must be noted about the migration of events, since we have many different regions of phase space in the analysis. The signal region and the sidebands have orthogonal kinematic requirements, so an event cannot enter the signal region *and* one of the sidebands. The same is true amongst the control regions, i.e., an event cannot enter more than one of them due to the designed orthogonality. An event *is* able to enter the signal region or a sideband with w_{veto} , and also one of the control regions with w_{sel} . Since events in data are not weighted, they may only enter a single region.

4.4 Triggers

4.5 Background estimation

4.5.1 Control regions

4.5.2 Sidebands to the signal region

4.5.3 Background estimation methods

SEARCH FOR DARK MATTER THROUGH THE PRODUCTION OF SEMI-VISIBLE JETS

This is the analysis chapter on semi-visible jets.

- Discuss how the theoretical aspects from the Theory chapter translate into an experimental search.
- Include object definitions, triggers, overall analysis strategy, signal production, event selection, background estimation and results/limit (including comparisons to similar searches – monojet/dijet exotic searches).
- Emphasise my contributions: s - and t -channel signal model production and understanding, Angular variable study for QCD background rejection (if used).
- Current material: no public plots as of yet. Hope to finish s -channel analysis soon (see previous section for caveats regarding inclusion), no timeline on t -channel analysis.

5.1 Analysis overview

5.2 Data and simulation

5.2.1 Generating signal samples in PYTHIA

5.2.2 Generating signal samples in MADGRAPH

5.2.3 Triggers

5.3 Background estimation

CONCLUSIONS

This is the conclusion.

Include a summary of thesis and work done over the course of my PhD with emphasis on the most important results/contributions.

- Mention the direction the semi-visible jet and Higgs to invisible analyses can take (sharing ideas/strategies I have, potential improvements with more LHC data and future prospects from potential future experiments).
 - SVJ has the t-channel and boosted searches underway, so those could yield interesting results. Long-lived searches are also an option. Higher energy collider like FCC gives larger range of phase space to explore
 - For Higgs to invisible, precision collider like FCC-ee or ILC might be required to actually observe the process (assuming it's BR is around SM value). Otherwise, we just need a lot of LHC data to narrow down the BR if it is enhanced by some BSM process.
 - Both searches can be improved with better ML techniques and stuff for categorisation/background rejection.

Begins an appendix

A P P E N D I X



APPENDIX A

BIBLIOGRAPHY

- [1] S. (UKRI), *CERN Accelerator Complex*, URL: <https://stfc.ukri.org/research/particle-physics-and-particle-astrophysics/large-hadron-collider/cern-accelerator-complex/> (visited on 22/03/2020).
- [2] M. AABOUD et al., *Performance of the ATLAS Track Reconstruction Algorithms in Dense Environments in LHC Run 2*, Eur. Phys. J. C77.10 (2017), p. 673, doi: [10.1140/epjc/s10052-017-5225-7](https://doi.org/10.1140/epjc/s10052-017-5225-7), arXiv: [1704.07983 \[hep-ex\]](https://arxiv.org/abs/1704.07983).
- [3] M. AABOUD et al., *Combination of searches for invisible Higgs boson decays with the ATLAS experiment*, Submitted to: Phys. Rev. Lett. (2019), arXiv: [1904.05105 \[hep-ex\]](https://arxiv.org/abs/1904.05105).
- [4] M. AABOUD et al., *Observation of $H \rightarrow b\bar{b}$ decays and VH production with the ATLAS detector*, Phys. Lett. B786 (2018), pp. 59–86, doi: [10.1016/j.physletb.2018.09.013](https://doi.org/10.1016/j.physletb.2018.09.013), arXiv: [1808.08238 \[hep-ex\]](https://arxiv.org/abs/1808.08238).
- [5] G. AAD et al., *Observation of a new particle in the search for the Standard Model Higgs boson with the ATLAS detector at the LHC*, Phys. Lett. B716 (2012), pp. 1–29, doi: [10.1016/j.physletb.2012.08.020](https://doi.org/10.1016/j.physletb.2012.08.020), arXiv: [1207.7214 \[hep-ex\]](https://arxiv.org/abs/1207.7214).
- [6] R. AAIJ et al., *Measurement of the inelastic pp cross-section at a centre-of-mass energy of 13 TeV*, JHEP 06 (2018), p. 100, doi: [10.1007/JHEP06\(2018\)100](https://doi.org/10.1007/JHEP06(2018)100), arXiv: [1803.10974 \[hep-ex\]](https://arxiv.org/abs/1803.10974).
- [7] D. ABERCROMBIE et al., *Dark Matter Benchmark Models for Early LHC Run-2 Searches: Report of the ATLAS/CMS Dark Matter Forum*, Phys. Dark Univ. 27 (2020), ed. by A. BOVEIA et al., p. 100371, doi: [10.1016/j.dark.2019.100371](https://doi.org/10.1016/j.dark.2019.100371), arXiv: [1507.00966 \[hep-ex\]](https://arxiv.org/abs/1507.00966).
- [8] N. AGHANIM et al., *Planck 2018 results. VI. Cosmological parameters* (2018), arXiv: [1807.06209 \[astro-ph.CO\]](https://arxiv.org/abs/1807.06209).

BIBLIOGRAPHY

- [9] S. AGOSTINELLI et al., *Geant4—a simulation toolkit*, Nuclear Instruments and Methods in Physics Research Section A: Accelerators, Spectrometers, Detectors and Associated Equipment 506.3 (2003), pp. 250–303, ISSN: 0168-9002, doi: [https://doi.org/10.1016/S0168-9002\(03\)01368-8](https://doi.org/10.1016/S0168-9002(03)01368-8).
- [10] D. S. AKERIB et al., *The LUX-ZEPLIN (LZ) Experiment*, Nucl. Instrum. Meth. A953 (2020), p. 163047, doi: [10.1016/j.nima.2019.163047](https://doi.org/10.1016/j.nima.2019.163047), arXiv: [1910.09124 \[physics.ins-det\]](https://arxiv.org/abs/1910.09124).
- [11] J. A. et. al., *Recent developments in Geant4*, Nuclear Instruments and Methods in Physics Research Section A: Accelerators, Spectrometers, Detectors and Associated Equipment 835 (2016), pp. 186–225, ISSN: 0168-9002, doi: <https://doi.org/10.1016/j.nima.2016.06.125>.
- [12] J. ALLISON et al., *Geant4 developments and applications*, IEEE Transactions on Nuclear Science 53.1 (Feb. 2006), pp. 270–278, ISSN: 1558-1578, doi: [10.1109/TNS.2006.869826](https://doi.org/10.1109/TNS.2006.869826).
- [13] J. ALWALL et al., *The automated computation of tree-level and next-to-leading order differential cross sections, and their matching to parton shower simulations*, JHEP 07 (2014), p. 079, doi: [10.1007/JHEP07\(2014\)079](https://doi.org/10.1007/JHEP07(2014)079), arXiv: [1405.0301 \[hep-ph\]](https://arxiv.org/abs/1405.0301).
- [14] G. APOLLINARI et al., *High Luminosity Large Hadron Collider HL-LHC*, CERN Yellow Rep. 5 (2015), pp. 1–19, doi: [10.5170/CERN-2015-005.1](https://doi.org/10.5170/CERN-2015-005.1), arXiv: [1705.08830 \[physics.acc-ph\]](https://arxiv.org/abs/1705.08830).
- [15] G. APOLLINARI et al., *High-Luminosity Large Hadron Collider (HL-LHC): Technical Design Report V. 0.1*, CERN Yellow Reports: Monographs, CERN, Geneva, 2017, doi: [10.23731/CYRM-2017-004](https://doi.org/10.23731/CYRM-2017-004).
- [16] G. ARCADI, A. DJOUADI and M. RAIDAL, *Dark Matter through the Higgs portal*, Phys. Rept. 842 (2020), pp. 1–180, doi: [10.1016/j.physrep.2019.11.003](https://doi.org/10.1016/j.physrep.2019.11.003), arXiv: [1903.03616 \[hep-ph\]](https://arxiv.org/abs/1903.03616).
- [17] G. ARNISON et al., *Experimental observation of isolated large transverse energy electrons with associated missing energy at $\sqrt{s} = 540 \text{ GeV}$* , Physics Letters B 122.1 (1983), pp. 103–116, ISSN: 0370-2693, doi: [https://doi.org/10.1016/0370-2693\(83\)91177-2](https://doi.org/10.1016/0370-2693(83)91177-2).
- [18] G. ARNISON et al., *Experimental Observation of Lepton Pairs of Invariant Mass Around 95- GeV/c^{**2} at the CERN SPS Collider*, Phys. Lett. 126B (1983), pp. 398–410, doi: [10.1016/0370-2693\(83\)90188-0](https://doi.org/10.1016/0370-2693(83)90188-0).

- [19] P. ATHRON et al., *Global analyses of Higgs portal singlet dark matter models using GAMBIT*, The European Physical Journal C 79.1 (2019), p. 38, doi: [10.1140/epjc/s10052-018-6513-6](https://doi.org/10.1140/epjc/s10052-018-6513-6).
- [20] P. BAGNAIA et al., *Evidence for $Z^0 \rightarrow e^+ e^-$ at the CERN anti- $p\bar{p}$ Collider*, Phys. Lett. 129B (1983), pp. 130–140, doi: [10.1016/0370-2693\(83\)90744-X](https://doi.org/10.1016/0370-2693(83)90744-X).
- [21] I. BALDES and K. PETRAKI, *Asymmetric thermal-relic dark matter: Sommerfeld-enhanced freeze-out, annihilation signals and unitarity bounds* (2017), arXiv: [1703.00478 \[hep-ph\]](https://arxiv.org/abs/1703.00478).
- [22] M. BANNER et al., *Observation of single isolated electrons of high transverse momentum in events with missing transverse energy at the CERN pp collider*, Physics Letters B 122.5 (1983), pp. 476–485, issn: 0370-2693, doi: [https://doi.org/10.1016/0370-2693\(83\)91605-2](https://doi.org/10.1016/0370-2693(83)91605-2).
- [23] G. BATTAGLIA et al., *Erratum: The radial velocity dispersion profile of the Galactic halo: constraining the density profile of the dark halo of the Milky Way*, Mon. Not. R. Astron. Soc. 370.2 (Aug. 2006), pp. 1055–1056, doi: [10.1111/j.1365-2966.2006.10688.x](https://doi.org/10.1111/j.1365-2966.2006.10688.x).
- [24] G. BATTAGLIA et al., *The radial velocity dispersion profile of the Galactic halo: constraining the density profile of the dark halo of the Milky Way*, Mon. Not. R. Astron. Soc. 364.2 (Dec. 2005), pp. 433–442, doi: [10.1111/j.1365-2966.2005.09367.x](https://doi.org/10.1111/j.1365-2966.2005.09367.x), arXiv: [astro-ph/0506102 \[astro-ph\]](https://arxiv.org/abs/astro-ph/0506102).
- [25] G. L. BAYATYAN et al., *CMS TriDAS project: Technical Design Report, Volume 1: The Trigger Systems*, Technical Design Report CMS.
- [26] C. M. BENDER and S. SARKAR, *Asymptotic Analysis of the Boltzmann Equation for Dark Matter Relics*, J. Math. Phys. 53 (2012), p. 103509, doi: [10.1063/1.4753990](https://doi.org/10.1063/1.4753990), arXiv: [1203.1822 \[hep-th\]](https://arxiv.org/abs/1203.1822).
- [27] M. BENEDIKT, D. SCHULTE and F. ZIMMERMANN, *Optimizing integrated luminosity of future hadron colliders*, Phys. Rev. Spec. Top. Accel. Beams 18.CERN-ACC-2015-0166. 10 (Oct. 2015), 101002. 19 p, doi: [10.1103/PhysRevSTAB.18.101002](https://doi.org/10.1103/PhysRevSTAB.18.101002).
- [28] P. BEVINGTON and D. ROBINSON, *Data Reduction and Error Analysis for the Physical Sciences*, McGraw-Hill Higher Education, McGraw-Hill Education, 2003, ISBN: 9780072472271.

BIBLIOGRAPHY

- [29] P. BHATTACHARJEE et al., *Sizing-up the WIMPs of Milky Way : Deriving the velocity distribution of Galactic Dark Matter particles from the rotation curve data*, Phys. Rev. D87 (2013), p. 083525, doi: [10.1103/PhysRevD.87.083525](https://doi.org/10.1103/PhysRevD.87.083525), arXiv: [1210.2328 \[astro-ph.GA\]](https://arxiv.org/abs/1210.2328).
- [30] P. BLOCH et al., *Changes to CMS ECAL electronics: addendum to the Technical Design Report*, Technical Design Report CMS, CERN, Geneva, 2002.
- [31] A. BOVEIA and C. DOGLIONI, *Dark Matter Searches at Colliders*, Ann. Rev. Nucl. Part. Sci. 68 (2018), pp. 429–459, doi: [10.1146/annurev-nucl-101917-021008](https://doi.org/10.1146/annurev-nucl-101917-021008), arXiv: [1810.12238 \[hep-ex\]](https://arxiv.org/abs/1810.12238).
- [32] A. H. BROEILS, *The mass distribution of the dwarf spiral NGC 1560*, Astronomy & Astrophysics 256 (Mar. 1992), pp. 19–32.
- [33] O. S. BRÜNING et al., *LHC Design Report*, CERN Yellow Reports: Monographs, CERN, Geneva, 2004, doi: [10.5170/CERN-2004-003-V-1](https://doi.org/10.5170/CERN-2004-003-V-1).
- [34] M. CACCIARI, G. P. SALAM and G. SOYEZ, *The Anti- $k(t)$ jet clustering algorithm*, JHEP 04 (2008), p. 063, doi: [10.1088/1126-6708/2008/04/063](https://doi.org/10.1088/1126-6708/2008/04/063), arXiv: [0802.1189 \[hep-ph\]](https://arxiv.org/abs/0802.1189).
- [35] A. CANEPA, *Searches for supersymmetry at the Large Hadron Collider*, Reviews in Physics 4 (2019), p. 100033, ISSN: 2405-4283, doi: <https://doi.org/10.1016/j.revip.2019.100033>.
- [36] D. G. CERDEÑO et al., *B anomalies and dark matter: a complex connection*, The European Physical Journal C 79.6 (2019), p. 517, doi: [10.1140/epjc/s10052-019-6979-x](https://doi.org/10.1140/epjc/s10052-019-6979-x).
- [37] S. CHATRHYAN et al., *Description and performance of track and primary-vertex reconstruction with the CMS tracker*, JINST 9.10 (2014), P10009, doi: [10.1088/1748-0221/9/10/P10009](https://doi.org/10.1088/1748-0221/9/10/P10009), arXiv: [1405.6569 \[physics.ins-det\]](https://arxiv.org/abs/1405.6569).
- [38] S. CHATRHYAN et al., *Observation of a New Boson at a Mass of 125 GeV with the CMS Experiment at the LHC*, Phys. Lett. B716 (2012), pp. 30–61, doi: [10.1016/j.physletb.2012.08.021](https://doi.org/10.1016/j.physletb.2012.08.021), arXiv: [1207.7235 \[hep-ex\]](https://arxiv.org/abs/1207.7235).
- [39] S. CITTOLIN, A. RÁCZ and P. SPHICAS, *CMS The TriDAS Project: Technical Design Report, Volume 2: Data Acquisition and High-Level Trigger. CMS trigger and data-acquisition project*, Technical Design Report CMS, CERN, Geneva, 2002.

- [40] D. CLOWE, A. GONZALEZ and M. MARKEVITCH, *Weak-Lensing Mass Reconstruction of the Interacting Cluster 1E 0657-558: Direct Evidence for the Existence of Dark Matter*, The Astrophysical Journal 604.2 (2004), p. 596.
- [41] T. COHEN, M. LISANTI and H. K. LOU, *Semi-visible Jets: Dark Matter Undercover at the LHC*, Phys. Rev. Lett. 115.17 (2015), p. 171804, doi: [10.1103/PhysRevLett.115.171804](https://doi.org/10.1103/PhysRevLett.115.171804), arXiv: [1503.00009 \[hep-ph\]](https://arxiv.org/abs/1503.00009).
- [42] T. COHEN et al., *LHC Searches for Dark Sector Showers*, JHEP 11 (2017), p. 196, doi: [10.1007/JHEP11\(2017\)196](https://doi.org/10.1007/JHEP11(2017)196), arXiv: [1707.05326 \[hep-ph\]](https://arxiv.org/abs/1707.05326).
- [43] C. COLLABORATION, *CMS Luminosity Public Results*, URL: <https://twiki.cern.ch/twiki/bin/view/CMSPublic/LumiPublicResults> (visited on 22/02/2020).
- [44] C. COLLABORATION, *Luminosity Physics Object Group (Lumi POG)*, access may be restricted, URL: <https://twiki.cern.ch/twiki/bin/viewauth/CMS/TWikiLUM> (visited on 16/03/2020).
- [45] C. COLLABORATION, *Particle-Flow Event Reconstruction in CMS and Performance for Jets, Taus, and MET*, tech. rep. CMS-PAS-PFT-09-001, CERN, Geneva, Apr. 2009.
- [46] C. COLLABORATION, *The CMS electromagnetic calorimeter project: Technical Design Report*, Technical Design Report CMS, CERN, Geneva, 1997.
- [47] C. COLLABORATION, *The CMS hadron calorimeter project: Technical Design Report*, Technical Design Report CMS, CERN, Geneva, 1997.
- [48] C. COLLABORATION, *The CMS magnet project: Technical Design Report*, Technical Design Report CMS, CERN, Geneva, 1997.
- [49] C. COLLABORATION, *The CMS tracker: addendum to the Technical Design Report*, Technical Design Report CMS, CERN, Geneva, 2000.
- [50] J. CONRAD and O. REIMER, *Indirect dark matter searches in gamma and cosmic rays*, Nature Phys. 13.3 (2017), pp. 224–231, doi: [10.1038/nphys4049](https://doi.org/10.1038/nphys4049), arXiv: [1705.11165 \[astro-ph.HE\]](https://arxiv.org/abs/1705.11165).
- [51] B. COX and J. FORSHAW, *Universal: A Journey Through the Cosmos*, Penguin Books Limited, 2016, ISBN: 9780141968346.
- [52] M. DELLA NEGRA et al., *CMS: letter of intent by the CMS Collaboration for a general purpose detector at LHC*, tech. rep. CERN-LHCC-92-003. LHCC-I-1, Open presentation to the LHCC 5 November 1992, M. Della Negra/CERN, CMS Spokesman, CERN, Geneva, 1992.

BIBLIOGRAPHY

- [53] N. DEV et al., *The CMS Level-1 electron and photon trigger: for Run II of LHC*, Journal of Instrumentation 12.02 (Feb. 2017), pp. C02014–C02014, DOI: [10.1088/1748-0221/12/02/c02014](https://doi.org/10.1088/1748-0221/12/02/c02014).
- [54] A. DJOUADI et al., *Direct Detection of Higgs-Portal Dark Matter at the LHC*, Eur. Phys. J. C73.6 (2013), p. 2455, DOI: [10.1140/epjc/s10052-013-2455-1](https://doi.org/10.1140/epjc/s10052-013-2455-1), arXiv: [1205.3169 \[hep-ph\]](https://arxiv.org/abs/1205.3169).
- [55] M. DREWES, *The Phenomenology of Right Handed Neutrinos*, International Journal of Modern Physics E 22.08 (2013), p. 1330019, DOI: [10.1142/S0218301313300191](https://doi.org/10.1142/S0218301313300191).
- [56] J. EINASTO, *Dark Matter*, ArXiv e-prints (Jan. 2009), arXiv: [0901.0632 \[astro-ph.CO\]](https://arxiv.org/abs/0901.0632).
- [57] F. ENGLERT and R. BROUT, *Broken Symmetry and the Mass of Gauge Vector Mesons*, Phys. Rev. Lett. 13 (9 Aug. 1964), pp. 321–323, DOI: [10.1103/PhysRevLett.13.321](https://doi.org/10.1103/PhysRevLett.13.321).
- [58] V. FANTI et al., *A new measurement of direct CP violation in two pion decays of the neutral kaon*, Physics Letters B 465.1-4 (Oct. 1999), pp. 335–348, ISSN: 0370-2693, DOI: [10.1016/s0370-2693\(99\)01030-8](https://doi.org/10.1016/s0370-2693(99)01030-8).
- [59] B. D. FIELDS et al., *Big-Bang Nucleosynthesis After Planck*, JCAP 2003.03 (2020), p. 010, DOI: [10.1088/1475-7516/2020/03/010](https://doi.org/10.1088/1475-7516/2020/03/010), arXiv: [1912.01132 \[astro-ph.CO\]](https://arxiv.org/abs/1912.01132).
- [60] C. FINANCE and A. P. DEPARTMENT, *2020 Annual Contributions to CERN budget*, URL: <https://fap-dep.web.cern.ch/rpc/2020-annual-contributions-cern-budget> (visited on 30/03/2020).
- [61] K. C. FREEMAN, *On the Disks of Spiral and S0 Galaxies*, The Astrophysical Journal 160 (June 1970), p. 811, DOI: [10.1086/150474](https://doi.org/10.1086/150474).
- [62] S. FRIXIONE, P. NASON and C. OLEARI, *Matching NLO QCD computations with Parton Shower simulations: the POWHEG method*, JHEP 11 (2007), p. 070, DOI: [10.1088/1126-6708/2007/11/070](https://doi.org/10.1088/1126-6708/2007/11/070), arXiv: [0709.2092 \[hep-ph\]](https://arxiv.org/abs/0709.2092).
- [63] P. GONDOLO and G. GELMINI, *Cosmic Abundances of Stable Particles: improved analysis*, Nuclear Physics B - NUCL PHYS B 360 (Aug. 1991), pp. 145–179, DOI: [10.1016/0550-3213\(91\)90438-4](https://doi.org/10.1016/0550-3213(91)90438-4).
- [64] G. S. GURALNIK, C. R. HAGEN and T. W. B. KIBBLE, *Global Conservation Laws and Massless Particles*, Phys. Rev. Lett. 13 (20 Nov. 1964), pp. 585–587, DOI: [10.1103/PhysRevLett.13.585](https://doi.org/10.1103/PhysRevLett.13.585).
- [65] L. J. HALL et al., *Freeze-In Production of FIMP Dark Matter*, JHEP 03 (2010), p. 080, DOI: [10.1007/JHEP03\(2010\)080](https://doi.org/10.1007/JHEP03(2010)080), arXiv: [0911.1120 \[hep-ph\]](https://arxiv.org/abs/0911.1120).

- [66] T. HAN, Z. LIU and A. NATARAJAN, *Dark matter and Higgs bosons in the MSSM*, JHEP 11 (2013), p. 008, DOI: [10.1007/JHEP11\(2013\)008](https://doi.org/10.1007/JHEP11(2013)008), arXiv: [1303.3040 \[hep-ph\]](https://arxiv.org/abs/1303.3040).
- [67] T. HAN, J. D. LYKKEN and R.-J. ZHANG, *On Kaluza-Klein states from large extra dimensions*, Phys. Rev. D59 (1999), p. 105006, DOI: [10.1103/PhysRevD.59.105006](https://doi.org/10.1103/PhysRevD.59.105006), arXiv: [hep-ph/9811350 \[hep-ph\]](https://arxiv.org/abs/hep-ph/9811350).
- [68] F. HASERT et al., *Observation of neutrino-like interactions without muon or electron in the gargamelle neutrino experiment*, Physics Letters B 46.1 (1973), pp. 138–140, ISSN: 0370-2693, DOI: [https://doi.org/10.1016/0370-2693\(73\)90499-1](https://doi.org/10.1016/0370-2693(73)90499-1).
- [69] F. HASERT et al., *Search for elastic muon-neutrino electron scattering*, Physics Letters B 46.1 (1973), pp. 121–124, ISSN: 0370-2693, DOI: [https://doi.org/10.1016/0370-2693\(73\)90494-2](https://doi.org/10.1016/0370-2693(73)90494-2).
- [70] S. HEINEMEYER et al., *Handbook of LHC Higgs Cross Sections: 3. Higgs Properties: Report of the LHC Higgs Cross Section Working Group*, ed. by S. HEINEMEYER, CERN Yellow Reports: Monographs, July 2013.
- [71] W. HERR and B. MURATORI, *Concept of luminosity* (2006), DOI: [10.5170/CERN-2006-002.361](https://doi.org/10.5170/CERN-2006-002.361).
- [72] J. HERZOG-ARBEITMAN et al., *Empirical Determination of Dark Matter Velocities using Metal-Poor Stars*, Phys. Rev. Lett. 120.4 (2018), p. 041102, DOI: [10.1103/PhysRevLett.120.041102](https://doi.org/10.1103/PhysRevLett.120.041102), arXiv: [1704.04499 \[astro-ph.GA\]](https://arxiv.org/abs/1704.04499).
- [73] P. W. HIGGS, *Broken Symmetries and the Masses of Gauge Bosons*, Phys. Rev. Lett. 13 (16 Oct. 1964), pp. 508–509, DOI: [10.1103/PhysRevLett.13.508](https://doi.org/10.1103/PhysRevLett.13.508).
- [74] D. HUTERER, *Weak lensing, dark matter and dark energy*, General Relativity and Gravitation 42 (Sept. 2010), pp. 2177–2195, DOI: [10.1007/s10714-010-1051-z](https://doi.org/10.1007/s10714-010-1051-z), arXiv: [1001.1758 \[astro-ph.CO\]](https://arxiv.org/abs/1001.1758).
- [75] P. R. KAFLE et al., *On the Shoulders of Giants: Properties of the Stellar Halo and the Milky Way Mass Distribution*, Astrophys. J. 794.1 (2014), p. 59, DOI: [10.1088/0004-637X/794/1/59](https://doi.org/10.1088/0004-637X/794/1/59), arXiv: [1408.1787 \[astro-ph.GA\]](https://arxiv.org/abs/1408.1787).
- [76] M. KAKIZAKI et al., *Phenomenological constraints on light mixed sneutrino dark matter scenarios*, Physics Letters B 749 (2015), pp. 44–49, ISSN: 0370-2693, DOI: <https://doi.org/10.1016/j.physletb.2015.07.030>.
- [77] J. C. KAPTEYN, *First Attempt at a Theory of the Arrangement and Motion of the Sidereal System*, The Astrophysical Journal 55 (May 1922), p. 302, DOI: [10.1086/142670](https://doi.org/10.1086/142670).

BIBLIOGRAPHY

- [78] V. KARIMÄKI et al., *The CMS tracker system project: Technical Design Report*, Technical Design Report CMS, CERN, Geneva, 1997.
- [79] V. KHACHATRYAN et al., *A search for new phenomena in pp collisions at $\sqrt{s} = 13\text{ TeV}$ in final states with missing transverse momentum and at least one jet using the α_T variable*, Eur. Phys. J. C77.5 (2017), p. 294, doi: [10.1140/epjc/s10052-017-4787-8](https://doi.org/10.1140/epjc/s10052-017-4787-8), arXiv: [1611.00338 \[hep-ex\]](https://arxiv.org/abs/1611.00338).
- [80] V. KHACHATRYAN et al., *Search for dark matter, extra dimensions, and unparticles in monojet events in proton–proton collisions at $\sqrt{s} = 8\text{ TeV}$* , Eur. Phys. J. C75.5 (2015), p. 235, doi: [10.1140/epjc/s10052-015-3451-4](https://doi.org/10.1140/epjc/s10052-015-3451-4), arXiv: [1408.3583 \[hep-ex\]](https://arxiv.org/abs/1408.3583).
- [81] V. KHACHATRYAN et al., *Search for Microscopic Black Hole Signatures at the Large Hadron Collider*, Phys. Lett. B697 (2011), pp. 434–453, doi: [10.1016/j.physletb.2011.02.032](https://doi.org/10.1016/j.physletb.2011.02.032), arXiv: [1012.3375 \[hep-ex\]](https://arxiv.org/abs/1012.3375).
- [82] G. KRNJACIĆ, *Freezing In, Heating Up, and Freezing Out: Predictive Nonthermal Dark Matter and Low-Mass Direct Detection*, JHEP 10 (2018), p. 136, doi: [10.1007/JHEP10\(2018\)136](https://doi.org/10.1007/JHEP10(2018)136), arXiv: [1711.11038 \[hep-ph\]](https://arxiv.org/abs/1711.11038).
- [83] J. G. LAYTER, *The CMS muon project: Technical Design Report*, Technical Design Report CMS, CERN, Geneva, 1997.
- [84] M. LISANTI, *Lectures on Dark Matter Physics*, in: *Proceedings, Theoretical Advanced Study Institute in Elementary Particle Physics: New Frontiers in Fields and Strings (TASI 2015): Boulder, CO, USA, June 1-26, 2015*, 2017, pp. 399–446, doi: [10.1142/9789813149441_0007](https://doi.org/10.1142/9789813149441_0007), arXiv: [1603.03797 \[hep-ph\]](https://arxiv.org/abs/1603.03797).
- [85] S. P. MARTIN, *A Supersymmetry primer*, Adv. Ser. Direct. High Energy Phys 18 (1998), pp. 1–98, doi: [10.1142/9789812839657_0001](https://doi.org/10.1142/9789812839657_0001), [10.1142/9789814307505_0001](https://doi.org/10.1142/9789814307505_0001), arXiv: [hep-ph/9709356 \[hep-ph\]](https://arxiv.org/abs/hep-ph/9709356).
- [86] S. MERTENS, *Direct Neutrino Mass Experiments*, Journal of Physics: Conference Series 718.2 (2016), p. 022013.
- [87] J. MOUSA et al., *Overview of the CMS Detector Performance at LHC Run 2*, Universe 5 (Jan. 2019), p. 18.
- [88] K. NAKAMURA and P. D. GROUP, *Review of Particle Physics*, Journal of Physics G: Nuclear and Particle Physics 37.7A (2010), p. 075021.
- [89] P. NASON, *A New method for combining NLO QCD with shower Monte Carlo algorithms*, JHEP 11 (2004), p. 040, doi: [10.1088/1126-6708/2004/11/040](https://doi.org/10.1088/1126-6708/2004/11/040), arXiv: [hep-ph/0409146 \[hep-ph\]](https://arxiv.org/abs/hep-ph/0409146).

- [90] M. PERSIC, P. SALUCCI and F. STEL, *The universal rotation curve of spiral galaxies - I. The dark matter connection*, Mon. Not. R. Astron. Soc. 281 (July 1996), pp. 27–47, doi: [10.1093/mnras/281.1.27](https://doi.org/10.1093/mnras/281.1.27), eprint: [astro-ph/9506004](https://arxiv.org/abs/astro-ph/9506004).
- [91] T. SAKUMA, *Cutaway diagrams of CMS detector* (May 2019).
- [92] M. SCHUMANN, *Direct Detection of WIMP Dark Matter: Concepts and Status*, J. Phys. G46.10 (2019), p. 103003, doi: [10.1088/1361-6471/ab2ea5](https://doi.org/10.1088/1361-6471/ab2ea5), arXiv: [1903.03026 \[astro-ph.CO\]](https://arxiv.org/abs/1903.03026).
- [93] A. M. SIRUNYAN et al., *Observation of Higgs boson decay to bottom quarks*, Phys. Rev. Lett. 121.12 (2018), p. 121801, doi: [10.1103/PhysRevLett.121.121801](https://doi.org/10.1103/PhysRevLett.121.121801), arXiv: [1808.08242 \[hep-ex\]](https://arxiv.org/abs/1808.08242).
- [94] A. M. SIRUNYAN et al., *Particle-flow reconstruction and global event description with the CMS detector*, JINST 12 (2017), P10003, doi: [10.1088/1748-0221/12/10/P10003](https://doi.org/10.1088/1748-0221/12/10/P10003), arXiv: [1706.04965 \[physics.ins-det\]](https://arxiv.org/abs/1706.04965).
- [95] A. M. SIRUNYAN et al., *Search for natural and split supersymmetry in proton-proton collisions at $\sqrt{s} = 13$ TeV in final states with jets and missing transverse momentum*, Journal of High Energy Physics 2018.5 (May 2018), p. 25, doi: [10.1007/JHEP05\(2018\)025](https://doi.org/10.1007/JHEP05(2018)025).
- [96] A. M. SIRUNYAN et al., *Search for dijet resonances in proton-proton collisions at $\sqrt{s} = 13$ TeV and constraints on dark matter and other models*, Phys. Lett. B769 (2017), [Erratum: Phys. Lett.B772,882(2017)], pp. 520–542, doi: [10.1016/j.physletb.2017.09.029](https://doi.org/10.1016/j.physletb.2017.09.029), [10.1016/j.physletb.2017.02.012](https://doi.org/10.1016/j.physletb.2017.02.012), arXiv: [1611.03568 \[hep-ex\]](https://arxiv.org/abs/1611.03568).
- [97] A. M. SIRUNYAN et al., *Search for invisible decays of a Higgs boson produced through vector boson fusion in proton-proton collisions at $\sqrt{s} = 13$ TeV* (2018), arXiv: [1809.05937 \[hep-ex\]](https://arxiv.org/abs/1809.05937).
- [98] A. M. SIRUNYAN et al., *Search for new particles decaying to a jet and an emerging jet*, JHEP 02 (2019), p. 179, doi: [10.1007/JHEP02\(2019\)179](https://doi.org/10.1007/JHEP02(2019)179), arXiv: [1810.10069 \[hep-ex\]](https://arxiv.org/abs/1810.10069).
- [99] T. SJÖSTRAND et al., *An Introduction to PYTHIA 8.2*, Comput. Phys. Commun. 191 (2015), pp. 159–177, doi: [10.1016/j.cpc.2015.01.024](https://doi.org/10.1016/j.cpc.2015.01.024), arXiv: [1410.3012 \[hep-ph\]](https://arxiv.org/abs/1410.3012).
- [100] A. SOPCZAK, *Precision Measurements in the Higgs Sector at ATLAS and CMS*, PoS FFK2019.arXiv:2001.05927 (Jan. 2020), 006. 9 p, doi: [10.22323/1.353.0006](https://doi.org/10.22323/1.353.0006).

BIBLIOGRAPHY

- [101] M. J. STRASSLER and K. M. ZUREK, *Echoes of a hidden valley at hadron colliders*, Phys. Lett. B651 (2007), pp. 374–379, doi: [10.1016/j.physletb.2007.06.055](https://doi.org/10.1016/j.physletb.2007.06.055), arXiv: [hep-ph/0604261 \[hep-ph\]](https://arxiv.org/abs/hep-ph/0604261).
- [102] L. G. TRENTADUE et al., *Neutrino counting*, CERN-TH-5528-89 (Sept. 1989), 42 p, doi: [10.5170/CERN-1989-008-V-1.129](https://doi.org/10.5170/CERN-1989-008-V-1.129).
- [103] A. VICENTE, *Anomalies in $b \rightarrow s$ transitions and dark matter*, Advances in High Energy Physics 2018 (Mar. 2018), doi: [10.1155/2018/3905848](https://doi.org/10.1155/2018/3905848).
- [104] S. WEINBERG, *Cosmology*, Cosmology, OUP Oxford, 2008, ISBN: 9780191523601.
- [105] S. D. M. WHITE and M. J. REES, *Core condensation in heavy halos: a two-stage theory for galaxy formation and clustering*, Mon. Not. R. Astron. Soc. 183.3 (1978), p. 341, doi: [10.1093/mnras/183.3.341](https://doi.org/10.1093/mnras/183.3.341).
- [106] C. YOZIN and K. BEKKI, *The quenching and survival of ultra-diffuse galaxies in the Coma cluster*, Mon. Not. R. Astron. Soc. 452.1 (2015), pp. 937–943, doi: [10.1093/mnras/stv1073](https://doi.org/10.1093/mnras/stv1073), arXiv: [1507.05161 \[astro-ph.GA\]](https://arxiv.org/abs/1507.05161).
- [107] A. ZABI et al., *The CMS Level-1 Calorimeter Trigger for the LHC Run II*, Journal of Instrumentation 12.01 (Jan. 2017), pp. C01065–C01065, doi: [10.1088/1748-0221/12/01/c01065](https://doi.org/10.1088/1748-0221/12/01/c01065).

GLOSSARY

***b*-jet** A jet identified by a given algorithm or classifier as originating from a b quark.

PARTICLE FLOW algorithm An event reconstruction algorithm used in CMS. Information from all subdetectors is combined so that all stable particles can be identified. Jets are clustered, and complex objects such as b -jets are classified.

anti- k_{T} algorithm A sequential clustering algorithm designed to group hadronic particles into jets with a radius parameter (R). The transverse momentum is symbolised as k_{T} instead of p_{T} . In CMS, standard radius parameters are $R = 0.4$ and $R = 0.8$, referred to as AK4 and AK8 jets, respectively.

control region A region of phase space orthogonal to the signal region, typically by requiring an object that would otherwise be vetoed in the signal region. A control region enriched in a background process present in the signal region (such as $W(\rightarrow \ell\nu) + \text{jets}$) can be used to model its influence more accurately.

jet A collimated shower of hadronic particles. High momentum quarks and gluons fragment due to colour confinement; the resulting particles deposit energy in the detector very close to each other and is reconstructed as a single physics object called a jet.

luminosity Instantaneous luminosity is a measure of the collision rate in a particle accelerator (given in units of area per unit time). The integrated luminosity is the instantaneous luminosity integrated over time and is a metric for the total amount of data delivered by an accelerator or collected by a detector.

missing transverse energy The negative vector sum of the transverse momentum of all particles in a collider event. It is sometimes abbreviate to “MET”, and also referred to in literature as “missing transverse momentum” ($p_{\mathrm{T}}^{\mathrm{miss}}$).

GLOSSARY

pileup The term ascribed to additional proton-proton collisions during a bunch crossing.

Pileup interactions typically produce a large number of low-momentum particles.

semi-visible jet A shower of standard model and dark hadrons from the decay of a leptophobic Z' or Φ mediator that couples the hidden sector to the standard model.

sideband A region of phase space orthogonal to the signal region, typically by inverting kinematic requirements. Similar to a control region, a sideband enriched in a background present in the signal region (such as QCD) can be used to model it more accurately.

ACRONYMS

eV electron volt.

cmssw CMS SoftWare.

AEGIS Antihydrogen Experiment: Gravity, Interferometry, Spectroscopy.

ALICE A Large Ion Collider Experiment.

ATLAS A Toroidal LHC ApparatuS.

BSM beyond the standard model.

CERN *Organisation Européenne pour la Recherche Nucléaire* (European Organisation for Nuclear Research).

CMS Compact Muon Solenoid.

DAQ data acquisition.

ECAL electromagnetic calorimeter.

FASER ForwArd Search ExpeRiment.

FCC Future Circular Collider.

HCAL hadron calorimeter.

HF hadron forward calorimeter.

HL-LHC High Luminosity Large Hadron Collider.

HLT High-Level Trigger.

ACRONYMS

ISOLDE Isotope Separator On Line DEvice.

JEC jet energy corrections.

L1 Level-1.

L1T Level-1 Trigger.

LEP Large Electron-Positron Collider.

LHC Large Hadron Collider.

LO leading order.

LSP lightest supersymmetric particle.

LZ LUX-ZEPLIN.

MC Monte Carlo.

MoEDAL Monopole and Exotics Detector at the LHC.

MOND modified Newtonian dynamics.

PF Particle Flow.

PS Proton Synchrotron.

PSB Proton Synchrotron Booster.

QCD Quantum Chromodynamics.

SM standard model.

SPS Super Proton Synchrotron.

SUSY supersymmetry.

TOTEM TOTal Elastic and diffractive cross section Measurement.

VBF vector boson fusion.

WIMP Weakly Interacting Massive Particle.